




# MINERALOGY, GEOCHEMISTRY, AND GENESIS OF KAOLINITIC CLAYSTONE DEPOSITS IN THE DATONG COALFIELD, NORTHERN CHINA

LINSONG LIU<sup>1</sup>, QINFU LIU<sup>1</sup> \* , THOMAS ALGEO<sup>2,3,4</sup>, HAO ZHANG<sup>5</sup>, YONGJIE YANG<sup>1</sup>,  
GAOYU PENG<sup>1</sup>, SHUAI ZHANG<sup>1</sup>, HANLIE HONG<sup>2</sup>, AND DI LIU<sup>1</sup>

<sup>1</sup>College of Geoscience and Survey Engineering, China University of Mining and Technology, Beijing 100083, China

<sup>2</sup>Department of Geology, University of Cincinnati, Cincinnati, OH 45221-0013, USA

<sup>3</sup>State Key Laboratory of Biogeology and Environmental Geology, School of Earth Sciences, China University of Geosciences-Wuhan, Wuhan 430074, China

<sup>4</sup>State Key Laboratory of Geological Processes and Mineral Resources, China University of Geosciences-Wuhan, Wuhan 430074, China

<sup>5</sup>School of Chemical and Environmental Engineering, China University of Mining and Technology, Beijing 100083, China

**Abstract**—Gray-black kaolinitic claystones of industrial value are abundant in Upper Carboniferous–Lower Permian coal-bearing strata of the Datong Coalfield of northern China. The main types are tonsteins and cryptocrystalline kaolinitic claystones, distinguished by the thinness and greater crystallinity of kaolinite in the former and by the presence of detrital illite and authigenic pyrite in the latter. In order to determine the formation history of these two types of kaolinitic claystone, the petrological, mineralogical, and geochemical characteristics of borehole samples from the Upper Carboniferous Taiyuan Formation which comprises siliciclastics and coal seams deposited in a coastal environment, were analyzed. In addition to kaolinite, the claystones contain subordinate illite, quartz, pyrite, anatase, feldspar, siderite, and calcite. The tonsteins and cryptocrystalline kaolinitic claystones have different sources, as shown by petrographic data, elemental ratios, and chondrite-normalized rare earth element (REE) patterns. The volcanic origin of the tonsteins is revealed by an abundance of volcanic quartz and vitric fragments as well as  $Al_2O_3/TiO_2$ , Zr/Hf, and Nb/Ta ratios consistent with a felsic igneous source. Their REE fraction was derived from feldspars or micas of the parent rocks, and the fraction decreased with alteration of these minerals to kaolinite. The sedimentary origin of the cryptocrystalline kaolinitic claystones is revealed by an abundance of detrital quartz and illite grains derived from either granite or sedimentary upper crust, and by the total REE contents ( $\Sigma REE$ ) and  $(La/Yb)_N$  values which are consistent with granitic material. Their depositional environment was in a transitional (coastal) setting (as shown by intermediate Sr/Ba ratios) hosting an open acidic hydrologic system (as shown by high chemical index of alteration (CIA) values indicative of intensive chemical weathering) that was suboxic to anoxic (as shown by high U/Th ratios and trace-metal enrichment factors). The present chemistry of these claystones was thus controlled by a combination of parent rock type and diagenetic alteration.

**Keywords**—Coal Seam · Diagenesis · Kaolinite · Leaching · Taiyuan Formation · Tonstein

## INTRODUCTION

In recent years, due to the scarcity of kaolinite resources, kaolinitic claystone deposits in coal-bearing strata have been studied widely and exploited internationally. They are useful both scientifically as marker beds to assist with stratigraphic correlations in coal-bearing basins (Uysal et al. 2000; Burger et al. 2002; Arbuzov et al. 2016), and economically as raw materials in various industries because of their large kaolinite content and small impurity load (Ece et al. 2003; Nzeugang et al. 2018). Related research has shown that kaolinitic claystone deposits in coal-bearing strata are formed commonly by sedimentation or hydrothermal alteration (Bohor and Triplehorn 1993; Liu and Zhang 1997; Liu et al. 2001; Spears 2012; Erkoyun et al. 2017; Zhao et al. 2018). The most common formation process is alteration of terrigenous clastic clay, feldspar, mica, and volcanic vitric fragments to kaolinite through leaching of alkaline ions and silica in an acid peat swamp environment (Dominguez et al. 2008; Ding et al. 2009).

Hydrothermal activity can contribute to kaolinization and other forms of alteration of volcanic glass or minerals in coal-bearing strata (Dai et al. 2014; Erkoyun et al. 2019; Zhao et al. 2019).

Kaolinitic claystone is abundantly present in Upper Paleozoic coal-bearing strata in northern China. In the Datong Coalfield, such deposits are found in coal swamp basins of the Late Carboniferous–Early Permian period (He 2006; Huo 2013). The petrology and mineralogy (Liu 1984; Zhang 1992; Zhao and Zheng 1997; Liu et al. 2001; Zhou 2010; Yuan et al. 2011), and geochemistry (Zhu 1997; Liu et al. 1998; Zou et al. 2016; Liu and Zhang 1997) of these deposits have been studied and these studies have shown two main types of kaolinitic claystone in the Taiyuan Formation of the Datong Coalfield, namely cryptocrystalline kaolinitic claystone and tonstein. Although earlier studies inferred different origins for these two types of claystone, differences in their characteristics and how those differences relate to their putative origins have not been investigated comprehensively.

The aim of the present study was to investigate the petrological, mineralogical, and geochemical characteristics of cryptocrystalline kaolinitic claystone and tonstein in coal-bearing strata of the Datong Coalfield, northern China, with the goals of determining their sources and pathways of diagenetic alteration. In addition, this research sought to provide insights into the geochemical behavior and significant

\* E-mail address of corresponding author: lqf@cumb.edu.cn

DOI: 10.1007/s42860-020-00109-2

differences of major and trace elements in cryptocrystalline kaolinitic claystone and tonstein during kaolinization in coal-forming environments. Thus, the purpose of this study was to improve understanding of the formation mechanisms of different types of kaolinitic claystone associated with coal beds, with the ultimate goal of enhancing exploitation of these resources.

## GEOLOGICAL SETTING

### *Datong Coalfield*

The Datong Coalfield is located in the northwestern Datong Basin, northern China (Fig. 1). The coalfield is, at its farthest points, 85 km long (N–S) and 30 km wide (E–W), with a total area of 1900 km<sup>2</sup>. The geological structure of the study area is a large open syncline (Yuan et al. 2011; Xi and Zhao 2011). Faults have developed in this area, most of which are normal with dips of >65°. A small-scale lamprophyre intrusion occurred in the middle of the coalfield during the Triassic Period (Gong 2006). The coalfield has undergone many stages of uplift and subsidence during its history. The major strata in the Datong Coalfield are the Upper Carboniferous Benxi and Taiyuan Formations, Lower Permian Shanxi and Xiashihezi Formations, Upper Permian Shangshihezi Formation, and Jurassic strata (Zhou 2010). The Nanyangpo mine sampled in the present study is located in the southwestern part of the Datong Coalfield (Fig. 1).

The Shanxi and Taiyuan Formations, the two main coal-bearing units in the Datong Coalfield, contain a large number of claystone beds with a total thickness of 145 m (Fig. 2). The Shanxi Formation, which was deposited in a meandering river environment (Zhang and Zhao 1990), consists mainly of siltstone, sandstone, limestone, claystone, and the No. 4 Coal seam, with a coarse quartz sandstone layer in the lowermost part of the formation. The Upper Carboniferous Taiyuan Formation, which was deposited in fluvial and deltaic environments, has a thickness ranging from 80 to 100 m (Cheng et al. 2015; Wang et al. 2018; Wang and Guo 2020). It consists mainly of fine to coarse sandstone, siltstone, claystone, and several coal seams, of which the No. 3, 5, and 8 coals are the most important economically (Fig. 2). The coal seams are underlain by claystones with a thickness of 2–8 m, and are capped by thin sandy claystones with an average thickness of ~1 m. The thicker coal seams contain partings with thicknesses ranging from 0.01 to 0.3 m. The Benxi Formation, underlying the Taiyuan Formation, was deposited in tidal flat and lagoonal environments (Zhao and Zheng 1997). It consists of claystone, sandstone, and limestone, with bauxite occurring locally at the top of the formation (Fig. 2). It overlies unconformably the Ordovician strata.

In the Late Paleozoic, the northern margin of the North China Block and the Siberian–southern Mongolian Block underwent initial continent–continent collision. During this orogenic process, a depression was formed at the margin of the subduction zone of the North China Block, and the coal-bearing Datong Basin was formed (Li 1981; Han et al. 2014). This basin was occupied during the Late Carboniferous by delta environments with abundant peat swamps, which were

conducive to the formation of coal and coal-bearing claystone deposits (Huo 2013).

### *Study Units*

The study section can be divided into four units, with each unit consisting of a sequence from the roof to the floor of one specific coal seam: Unit 1 consists of the No. 3 Coal, roof, partings, and floor; Unit 2 of the No. 5 Coal, partings and floor; Unit 3 of the No. 8 Coal, roof, partings, and floor; and Unit 4 of the No. 9 Coal floor only.

*Unit 1.* The No. 3 Coal seam is 3–5 m thick and intercalated with partings that are kaolinitic claystone with thicknesses of 0.5–0.8 m. From top to bottom, the samples in Unit 1 consist of dark gray silty claystone, coal seams, black partings, and brown claystone (Fig. 3). A 0.5 to 1.0 m thick, dark gray silty claystone is the roof of No. 3 Coal seam and has a blocky structure (Fig. 4a). The bottom is a compacted blocky brown kaolinitic claystone (Fig. 4b) with an average thickness of ~5 m. Microscope and XRD investigations showed that the claystone samples in Unit 1 consist mainly of kaolinite and quartz with minor illite, siderite, feldspar, and calcite. The crystalline kaolinite grains are <0.1 mm wide, but kaolinite occurs mostly as a cryptocrystalline matrix (Fig. 4c). In addition, some platy kaolinite and spherulitic siderite are surrounded by matrix. Platy kaolinite was formed by alteration of feldspar, and the surface is brown because of disseminated iron (Fig. 4d). This unit also contains authigenic quartz, the particle size of which is generally <10 μm and which appears black in cathodoluminescence (CL) spectroscopy (Fig. 4m). Quartz grains with diameters of >100 μm and rounded edges are terrigenous clastic quartz, and their color under CL is brown (Gotze et al. 2001).

*Unit 2.* The No. 5 Coal seam has several partings in the upper and middle parts that are composed of gray-black kaolinitic and dark gray sandy claystone (Fig. 3). This unit is capped by thick sandstone and conglomerate beds. The coal seam is 8–10 m thick with a blocky structure, and the dark gray, 0.3–0.5 m thick, coarse kaolinitic claystone alternates with coal layers. The lower claystone layer is ~4 m thick, is characterized by shiny, blocky structures, and contains pyrite nodules (Fig. 4e). The mineralogy of Unit 2 claystones consists of kaolinite, illite, quartz, pyrite, and trace amounts of anatase. These claystones have a granular texture. The kaolinite crystals are vermicular, up to 2 mm wide, and are derived from alteration of mica or feldspar (Fig. 4f, g). This coarsely phenocrystalline kaolinite is cemented by a cryptocrystalline kaolinite matrix. The Hinckley Indices (HI; Table 1) of these coarsely phenocrystalline kaolinites, which were calculated from the XRD patterns of the clay fractions, are 1.02 to 1.16, which is consistent with well-ordered kaolinite. Quartz was detected in the lower part, but not in the upper part of this unit. In the lower part, the pyrite content is up to 53.3%, where it occurs as framboids in the claystones (Fig. 4e). The framboidal pyrite is an aggregate of euhedral spherical pyrites <1 μm in

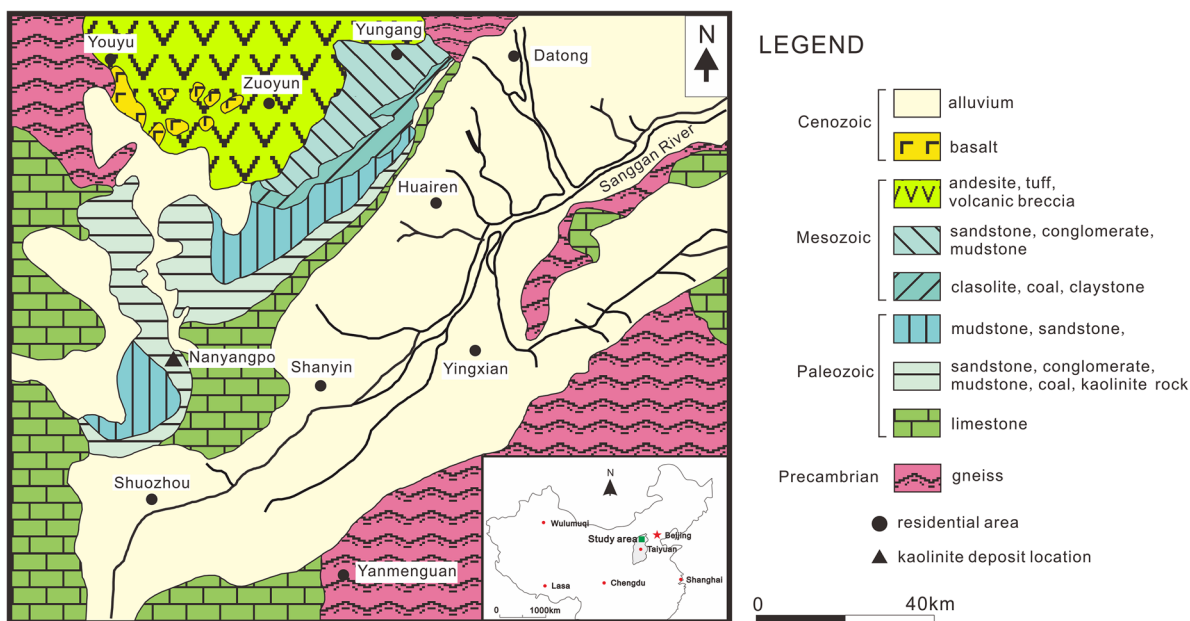


Fig. 1 Location and geological map of the Datong Basin, northern China and sample locations (modified from Gong 2006)

diameter, a form representing a syngenetic origin in the water column (Algeo et al. 2010; Wilkin and Barnes 1997).

**Unit 3.** The 3–5 m thick Unit 3 includes the No. 8 Coal seam roof, floor, and partings (Fig. 3). The coal has a blocky, shiny appearance and contains pyrite and intercalated organic-rich, hard, 0.2–0.6 m thick kaolinitic claystone layers (Fig. 4h). This unit is capped by a 0.5 m thick, dark gray, plastic, fine-grained claystone. The No. 8 Coal floor is a 1–3 m thick, dark brown, hard silty claystone. The main minerals in Unit 3 are kaolinite, quartz, and illite with minor amounts of feldspar, anatase, pyrite, siderite, and magnesite. Kaolinite occurs as a matrix, coating some terrigenous clastic quartz grains (Fig. 4i). Illite occurs as groundmass and has no obvious structure.

**Unit 4.** This unit contains both tonsteins and tuffaceous sandy claystones (Fig. 3). The upper part of this unit consists of a compact and massive, beige tonstein. The tonstein layers are 0.05–0.1 m thick and thinner than other claystone layers, such as kaolinitic claystone (0.5–5 m). These tonsteins are overlain by No. 9 Coal seam. The middle and lower parts of the unit contain a 5 m thick, dark gray, hard, blocky tuffaceous sandy claystone (Fig. 4j) which is composed dominantly of kaolinite with a smaller amount of quartz and trace amounts of siderite, magnesite, and anatase (Fig. 4k). Discrete kaolinite grains are of two types: (1) granular kaolinite similar to that of Unit 2; and (2) kaolinite aggregates with sizes of 1–3 mm, consisting of a cryptocrystalline kaolinite matrix and locally containing quartz crystal fragments and weakly recrystallized vitric fragments (Fig. 4l). The space between grains is filled with cryptocrystalline kaolinite matrix and tuffaceous clastic grains that are chert-like, recrystallized vitric fragments. The HI can reach 1.30 in this unit, indicating that the kaolinite is well ordered. Three types of quartz are present: terrigenous clastic grains,

volcaniclastic grains, and authigenic quartz (chert). The characteristics of the terrigenous clastic grains and authigenic quartz are similar to those of Unit 1. The volcaniclastic quartz grains are 0.5–1 mm in size, have angular to sub-angular shapes, and frequently show melted margins, indicating deposition as a welded tuff. Under CL, volcaniclastic quartz exhibits a blue-violet color, permitting it to be distinguished easily from other types of quartz (Fig. 4n,o). The amount of anatase in this unit is greater than in the other units, which is consistent with the general mineralogy of tonsteins (Price and Duff 1969). These anatases may have formed through decomposition of Ti-rich volcanic glass, ilmenite, magnetite, or rutile (Ruppert and Moore 1993).

## SAMPLES AND ANALYTICAL TECHNIQUES

A suite of 39 samples was collected from a drillcore of the Taiyuan Formation in the Nanyangpo mine of the Datong Coalfield including claystones, sandstones, conglomerates, coal, and partings (Fig. 3). Samples NP-6 to NP-12 are from Unit 1, samples NP-16 to NP-24 from Unit 2, samples NP-25 to NP-30 from Unit 3, and samples NP-32 to NP-39 from Unit 4. All bulk samples were made into thin sections for observation of petrological characteristics. A subset of samples ( $n = 30$ ) was crushed to powder with particle size of ~200 mesh using a tungsten carbide mill for mineralogical analyses, and 20 were selected for geochemical analysis.

Petrographic characterization of thin sections was carried out using a polarizing microscope (Nikon-LV 100Pol; Tokyo, Japan) at China University of Mining and Technology, Beijing, and a cathodoluminescence microscope (CL) (RELION CL VI; Bedford, Massachusetts, USA) at Petrochina Research Institute of Petroleum Exploration and Development. The CL microscope was operated at 13–15 kV, the current was 120–150  $\mu$ A, and

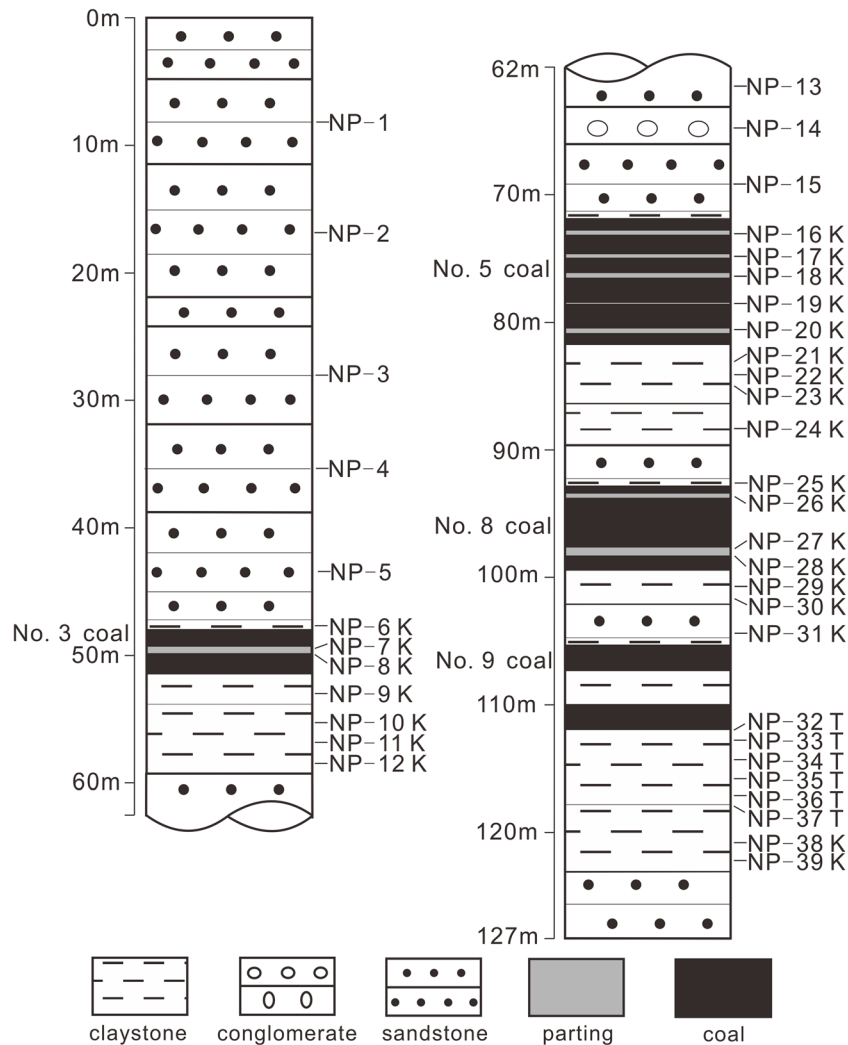
ERATHM	SYSTEM	SERIES	FORMATION	LITHOLOGY	EXPLANATION
Paleozoic	Permian	Lower Permian	Shanxi		
					siltstone, shale, claystone, limestone
					No.4 coal seam
					claystone, fine-grained sandstone, coarse sandstone
	Carboniferous	Upper Carboniferous	Taiyuan		shale, claystone, fine-grained sandstone, coarse sandstone
					No.2 coal seam
					claystone
					No.3 coal seam
					claystone, coarse sandstone, fine-grained sandstone, sandy claystone
					No.5 coal seam
					claystone, siltstone, fine-grained sandstone, sandy claystone
					No.8 coal seam
					claystone, coarse sandstone, fine-grained sandstone, sandy claystone
Carboniferous	Upper Carboniferous	Benxi		No.9 coal seam	
				tonstein, sandy claystone	
				bauxite, sandy claystone, sandstone, limestone	

Fig. 2 Stratigraphic section of the Datong Coalfield (modified from Huo 2013)

the exposure time was based on sample silicon content. Generally, exposure times were 60–80 s, but some areas with weak luminescence intensity required 100 s.

The whole-rock mineralogy of 30 samples was analyzed using an X-ray powder diffractometer (XRD) (Rigaku D/max-2500/PC; Tokyo, Japan) with Ni-filtered  $\text{CuK}\alpha$  radiation and a scintillation detector at China University of Mining and Technology, Beijing. The XRD patterns were recorded over an interval of  $2.5\text{--}70^\circ 2\theta$ , with a scan speed of  $2^\circ 2\theta \text{ min}^{-1}$ . Quantitative abundances of minerals in the bulk rock were obtained

using the adiabatic method of Brindley and Brown (1980). Clay minerals were identified after separation of the clay fraction by dispersion for 4 h in deionized water, followed by centrifugation. Clays were resuspended by ultrasonic vibration for 10 min, after which oriented mounts were prepared by dropping a small amount of suspension onto a glass slide and drying in air, solvating with ethylene glycol (EG) vapor at  $30^\circ\text{C}$  for 8 h, and heating at  $450^\circ\text{C}$  for 2.5 h. Relative abundances of minerals in the clay fraction were determined using



**Fig. 3** Simple stratigraphic histogram of the Nanyangpo mine and location of collected samples; K: cryptocrystalline kaolinitic claystone, T: tonstein

their typical reflections and the mineral intensity factors of Moore and Reynolds (1989).

In order to examine the microtextures of the claystones, SEM analysis was carried out using a HitachiS-4800 (Tokyo, Japan) Scanning Electron Microscope (SEM) equipped with an EDAX Genesis energy dispersive spectrometer (EDS) at the Beijing Center for Physical and Chemical Analysis. Quantitative EDS analyses were obtained from gold-coated polished thin sections of selected samples using a Si(Li) detector.

Twenty samples were selected for chemical analyses, including 16 cryptocrystalline kaolinitic claystone samples and four tonstein samples. (The tonstein beds were limited in number and thin and, therefore, difficult to sample.) Chemical analyses were carried out at the Beijing Center for Physical and Chemical Analysis. X-ray fluorescence spectrometry (XRF) (XRF-1800; Tokyo, Japan) was employed to determine the amounts of major element oxides. Concentrations of most trace elements were determined by inductively coupled plasma-mass spectrometry

(ICP-MS) on an ELEMENT XR (Thermo Fisher Scientific, Waltham, Massachusetts, USA) after digestion of sample powders. The digestion reagent was a mixture of 4 mL of 65% HNO<sub>3</sub> and 5 mL of 40% HF applied to 100 mg of each sample. This method has been proven to result in complete sample digestion for REEs (Dai et al. 2011). The detection limits for the analyses were between 0.01 and 0.1 wt.% for major elements, 0.1 to 5 ppm for trace elements, and 0.01 to 0.5 ppm for REEs. Loss on ignition (LOI) was determined as the weight difference after ignition at 900°C.

## RESULTS

### XRD Analysis

The mineralogical compositions of samples (Table 1) and the XRD results of whole-rock samples and clay fractions (Fig. 5) showed that the two types of

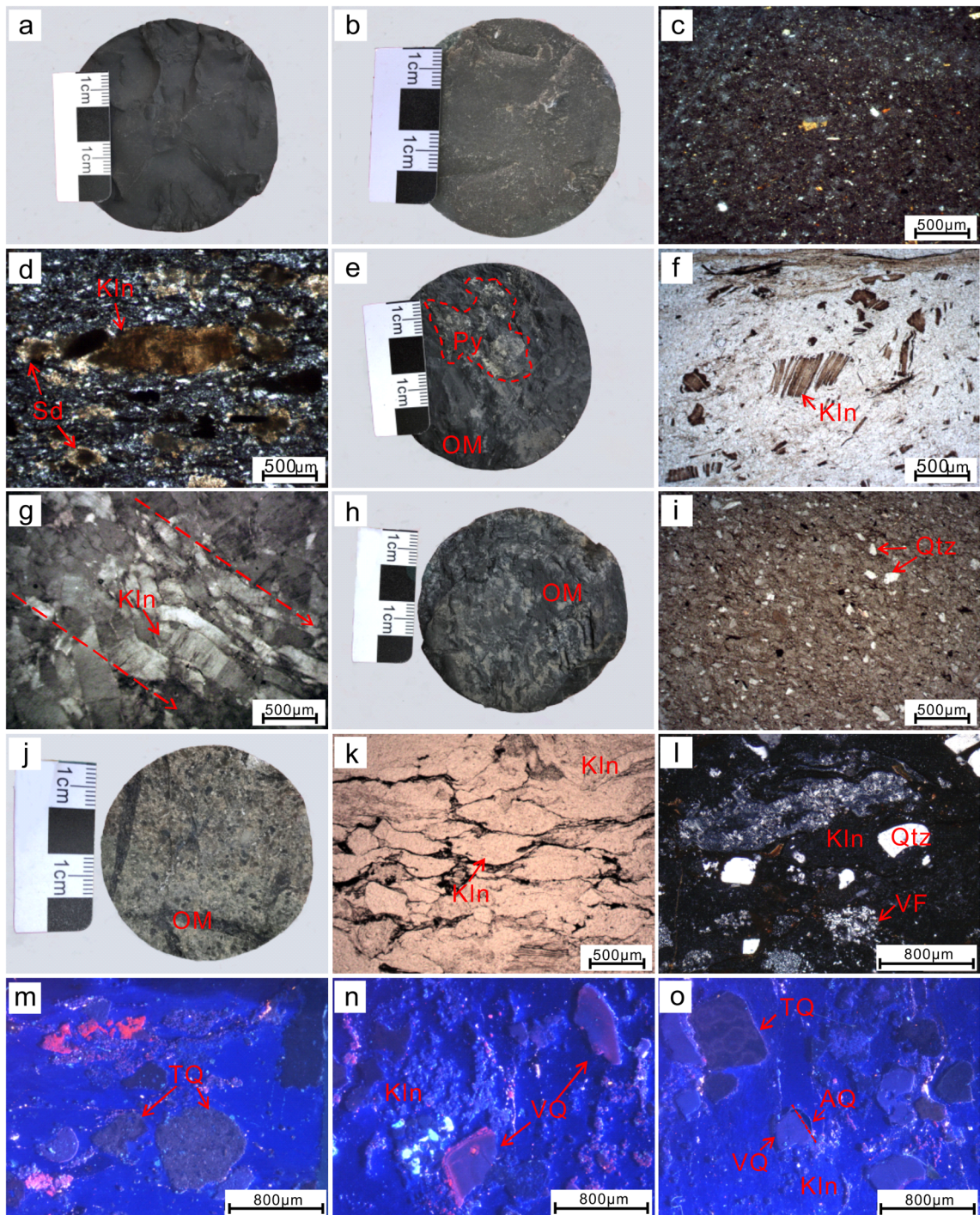


**Fig. 4** Photomicrographs of: **a** blocky structure, dark gray, silty claystone (Sample NP-7); **b** compact, blocky, brown claystone (Sample NP-9); **c, d** platy kaolinite and spherulitic siderite (Samples NP-7 and NP-10); **e** organic-rich claystone associated with pyrite (Sample NP-22); **f, g** mica and feldspar are mostly kaolinized and are cemented by a kaolinite matrix (Samples NP-17 and NP-20); **h** organic-rich, black claystone (Sample NP-26); **i** cryptocrystalline kaolinite with terrigenous clastic quartz (Sample NP-26); **j** dark gray, blocky, tuffaceous, sandy claystone (Sample NP-35); **k** kaolinite aggregates composed of cryptocrystalline kaolinite matrix (Sample NP-34); **l** quartz crystal fragments and weakly recrystallized vitric fragments (Sample NP-37); **m–o** brown terrigenous clastic quartz, blue-violet volcanic clastic quartz, and weakly or non-luminescent authigenic quartz (Samples NP-10 and NP-37); Kln: kaolinite; Qz: quartz; Py: pyrite; Sd: siderite; OM: organic matter; VF: recrystallized vitric fragments; TQ: terrigenous clastic quartz; VQ: volcanic clastic quartz; AQ: authigenic quartz

**Table 1** Mineral composition and relative contents (%) of the samples from Nanyangpo mine

Sample no.	Kaolinite	Quartz	Illite	Pyrite	Siderite	Feldspar	Anatase	Calcite	HI
NP-6	61.8	34.9	1.6	–	–	1.7	–	–	1.18
NP-7	84.1	8.3	7.5	–	–	–	–	0.1	0.63
NP-8	83.5	16.1	0.4	–	–	–	–	–	0.78
NP-9	77.2	10.0	9.1	–	3.5	–	0.2	–	0.80
NP-10	74.9	19.2	–	–	4.6	–	–	1.3	1.18
NP-11	75.2	19.4	–	–	2.7	0.6	–	2.1	1.26
NP-12	50.3	41	–	–	5.8	1.4	–	1.5	0.75
NP-16	69.9	–	–	30	–	–	–	0.1	1.16
NP-17	99.8	–	–	–	–	–	0.2	–	0.86
NP-18	99.6	–	–	–	–	–	0.4	–	1.07
NP-19	98.9	–	–	–	–	–	1.1	–	1.02
NP-20	99.4	–	–	–	–	–	0.6	–	1.10
NP-21	79.8	12.4	4.3	1.7	–	0.5	1.3	–	0.87
NP-22	58.4	13.3	3.1	25.2	–	0.1	–	–	0.81
NP-23	33.4	10.2	2.3	53.3	0.4	–	0.4	–	0.79
NP-24	55.9	32.5	5.0	4.4	–	2.1	–	–	0.73
NP-25	61.0	19.8	7.2	11.6	–	–	0.9	–	0.79
NP-26	62.8	21.2	8.0	7.0	–	0.4	0.6	–	0.81
NP-27	90.1	3.5	3.6	–	2.1	–	0.7	–	0.65
NP-28	80.4	5.1	10.2	–	3.4	0.3	0.6	–	0.64
NP-29	58.9	30.8	6.9	–	–	1.3	2.1	–	0.61
NP-30	52.0	40.1	5.1	–	–	0.2	2.6	–	0.61
NP-32	76.2	20.1	–	–	–	–	3.7	–	0.70
NP-33	81.3	16.5	–	–	–	–	2.2	–	1.15
NP-34	75.9	19.9	–	–	2.4	–	1.8	–	1.08
NP-35	74.4	22.6	–	–	0.6	–	2.3	–	1.00
NP-36	69.3	35.7	–	–	1.9	0.4	2.7	–	0.80
NP-37	75.7	19.3	–	–	3.0	–	2.0	–	1.30
NP-38	75.3	21.5	–	0.5	–	–	2.7	–	0.76
NP-39	44.7	50.8	–	–	0.4	–	4.1	–	0.74

–: not determined.

claystones (cryptocrystalline kaolinitic claystone and tonstein) have similar mineralogical assemblages, consisting mainly of kaolinite with minor quartz, anatase, feldspar, and siderite. The main difference between the two types is that illite and pyrite are limited to the cryptocrystalline kaolinitic claystones.

Kaolinite was identified based on its typical peaks at 7.15 Å and 3.58 Å, the absence of swelling with ethylene-glycol treatment, and by weakening of the 7.15 Å peak at temperatures above 450°C (Fig. 5). Well-ordered phases display sharp and strong peaks, whereas disordered phases exhibit broad and weak peaks in the XRD patterns. This feature suggests that kaolinite in the tonsteins generally exhibits a higher degree of ordering than that in the cryptocrystalline kaolinitic claystones. Illite was identified by characteristic peaks at 10 Å in the XRD patterns of the clay fractions.

#### SEM-EDS Analysis

The SEM observations showed that kaolinite in the claystones had various morphologies and crystal sizes. Kaolinite occurred mainly as euhedral to subhedral hexagonal platy crystals with diameters of 0.5–4 µm (Fig. 6a), and these crystals formed a single layer or several layers joined irregularly, face-to-face, to form banded or ellipsoidal aggregates (Fig. 6b) or cryptocrystalline kaolinite matrix. Some quartz, mica, and feldspar grains were observed embedded in the cryptocrystalline kaolinite matrix. Kaolinite occurred also as vermiform crystal grains with diameters of 5–10 µm which in many places showed gaps between layers (Fig. 6c,e). Kaolinite crystals with this morphology were seen in both cryptocrystalline kaolinitic claystone and tonstein samples. The reticular anatase found in kaolinite fissures (Fig. 6d) may have precipitated following dissolution of unstable Ti-containing minerals

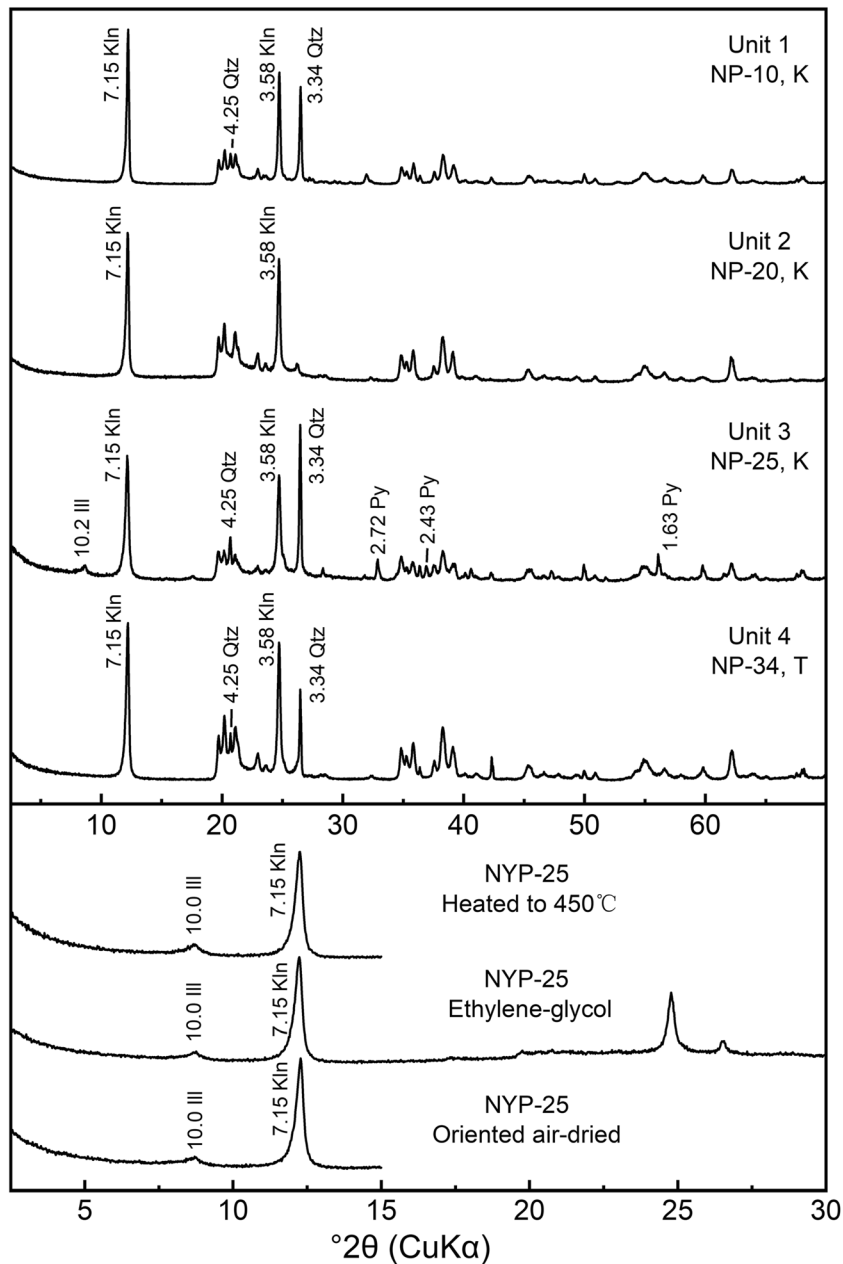


**Fig. 5** Typical XRD patterns of claystone samples in each section; Kln: kaolinite; Qtz: quartz; Ill: illite; Py: pyrite; K: cryptocrystalline kaolinitic claystone; T: tonstein

in the volcanic ash (Ruppert and Moore 1993; Triplehorn et al. 1991). The EDS analysis showed that the Fe content of the anatase was large (Fig. 6f), probably due to isomorphous substitution of Fe for Ti (Li 2015).

#### Concentration Profiles of Major Elements

The concentrations of major elements in the claystones of the units studied (Table 2) revealed that  $\text{Al}_2\text{O}_3$  and  $\text{SiO}_2$  contents ranged from 19.3 to 37.2 wt.% and 24.3 to 65.8 wt.%, respectively.  $\text{Al}_2\text{O}_3$  was enriched during alteration of K-feldspars, plagioclase, and volcanic glasses in the volcanic ash. The large

amount of  $\text{SiO}_2$  is due to the abundance of quartz and feldspar in the parent sediments. The present positive correlation of  $\text{Al}_2\text{O}_3$  with  $\text{SiO}_2$  ( $r = +0.68$ ,  $p < 0.01$ ) (Fig. 7) suggested that both oxides were present mainly in kaolinite. The ratios of  $\text{SiO}_2/\text{Al}_2\text{O}_3$  ranged from 1.18 to 1.83 in cryptocrystalline kaolinitic claystone samples and from 1.26 to 3.07 in tonstein samples, which were mostly higher than the theoretical value of kaolinite (1.18) (Kang 2015).

The  $\text{TiO}_2$  content of the study samples ranges from 0.12 to 2.21 wt.%, with significantly higher values in the tonsteins than in the cryptocrystalline kaolinitic claystones (Fig. 8) because of their greater anatase content. In contrast, the  $\text{TiO}_2$



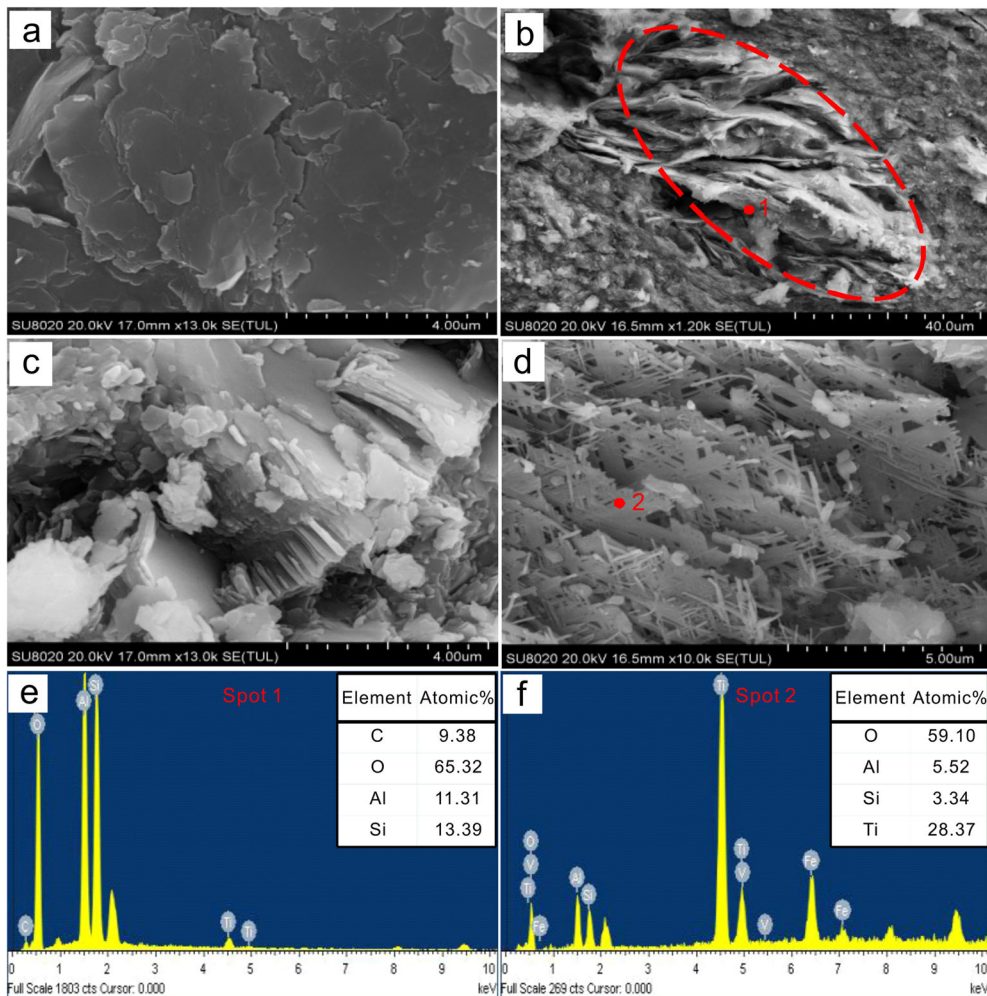


**Fig. 6** SEM images of: **a** euhedral to subhedral particles of kaolinite forming the rock matrix (Sample NP-18); **b** banded and ellipsoidal kaolinite aggregates surrounded by cryptocrystalline kaolinite matrix (Sample NP-34); **c** vermiform kaolinite crystal grain (Sample NP-17); **d** grid-like anatase in the kaolinite fissures (Sample NP-34); **e**, **f** EDS spectra of spots 1 and 2 (kaolinite and anatase, respectively).

content of coal-seam partings was smaller than that of the floors and roofs of coal seams, which conforms to the hypothesis of Liu and Zhang (1997) that organic acids in peat swamps can dissolve  $\text{TiO}_2$  in the partings. In the study samples,  $\text{TiO}_2$  does not show significant covariation with  $\text{Al}_2\text{O}_3$  (Table 4).

The amounts of  $\text{Na}_2\text{O}$  (avg. 0.05 wt.%),  $\text{MgO}$  (avg. 0.25 wt.%),  $\text{K}_2\text{O}$  (avg. 0.87 wt.%), and  $\text{CaO}$  (avg. 0.30 wt.%) in the four units were generally small. The  $\text{Fe}_2\text{O}_3$  content was largest in samples from the middle Taiyuan Formation (Fig. 8) owing to the presence of pyrite. Loss-on-ignition (LOI) values were 8.13–46.1 wt.%, with some organic-rich samples (especially coal partings) yielding greater LOI values.

#### Trace Elements in the Claystones

Trace-element enrichment factors in the claystones (EFs; Tribouvillard et al. 2006) were calculated as the ratio of the measured concentration of a particular element in a sample to its concentration in average upper continental

crust (Table 3) (Taylor and McLennan 1985; McLennan 2001). A number of trace elements were enriched significantly in the cryptocrystalline kaolinitic claystones of the study units, including Li, Cd, and Bi ( $\text{EF} > 2$ ) and Ga, In, Sb, Pb, Bi, Th, U, Nb, and Ta ( $1 < \text{EF} < 2$ ), but certain elements were depleted, including Be, V, Cr, Co, Ni, Rb, Cs, Sr, Ba, and Tl ( $\text{EF} < 0.5$ ). In contrast, only Li ( $\text{EF} > 2$ ) and Ga, Gd ( $1 < \text{EF} < 2$ ) were enriched in the tonsteins of the study area, other elements were depleted (Fig. 9). In order to determine whether compositional differences between the cryptocrystalline kaolinitic claystone and tonstein samples were meaningful, the Student's t-test was performed on these two types of samples on an element-by-element basis (Table 5). The result revealed significant differences between the two types of samples with respect to the major element oxides,  $\text{K}_2\text{O}$  and  $\text{Na}_2\text{O}$ , as well as the trace elements Be, Sc, Ga, Rb, Sb, Cs, Pb, Tl, Bi, Th, U, Nb, and Ta.

The high-field-strength elements (HFSE), including Zr, Hf, Nb, Ta, Th, and U, were enriched in most of the claystone

**Table 2** Major-element compositions (wt.%) of claystone samples in the study area, determined by XRF analysis

Major oxides (wt.%)	Section I samples										Section II samples										Section III samples										Section IV samples																																																	
	NP-7	NP-8	NP-9	NP-10	NP-11	NP-17	NP-18	NP-19	NP-21	NP-23	NP-25	NP-26	NP-27	NP-29	NP-30	NP-32	NP-33	NP-34	NP-37	NP-39	NP-7	NP-8	NP-9	NP-10	NP-11	NP-17	NP-18	NP-19	NP-21	NP-23	NP-25	NP-26	NP-27	NP-29	NP-30	NP-32	NP-33	NP-34	NP-37	NP-39	NP-7	NP-8	NP-9	NP-10	NP-11	NP-17	NP-18	NP-19	NP-21	NP-23	NP-25	NP-26	NP-27	NP-29	NP-30	NP-32	NP-33	NP-34	NP-37	NP-39	NP-7	NP-8	NP-9	NP-10	NP-11	NP-17	NP-18	NP-19	NP-21	NP-23	NP-25	NP-26	NP-27	NP-29	NP-30	NP-32	NP-33	NP-34	NP-37	NP-39
SiO <sub>2</sub>	35.28	48.48	51.89	51.49	53.12	43.91	39.71	28.65	42.04	24.26	44.55	39.27	42.32	54.13	53.32	46.63	48.96	52.10	52.28	55.81	35.28	48.48	51.89	51.49	53.12	43.91	39.71	28.65	42.04	24.26	44.55	39.27	42.32	54.13	53.32	46.63	48.96	52.10	52.28	55.81	35.28	48.48	51.89	51.49	53.12	43.91	39.71	28.65	42.04	24.26	44.55	39.27	42.32	54.13	53.32	46.63	48.96	52.10	52.28	55.81	35.28	48.48	51.89	51.49	53.12	43.91	39.71	28.65	42.04	24.26	44.55	39.27	42.32	54.13	53.32	46.63	48.96	52.10	52.28	55.81
Al <sub>2</sub> O <sub>3</sub>	25.58	34.81	28.40	31.08	31.06	37.18	30.84	24.14	33.37	19.34	29.35	26.84	34.14	32.29	32.60	36.97	34.63	32.17	31.44	31.46	25.58	34.81	28.40	31.08	31.06	37.18	30.84	24.14	33.37	19.34	29.35	26.84	34.14	32.29	32.60	36.97	34.63	32.17	31.44	31.46	25.58	34.81	28.40	31.08	31.06	37.18	30.84	24.14	33.37	19.34	29.35	26.84	34.14	32.29	32.60	36.97	34.63	32.17	31.44	31.46	25.58	34.81	28.40	31.08	31.06	37.18	30.84	24.14	33.37	19.34	29.35	26.84	34.14	32.29	32.60	36.97	34.63	32.17	31.44	31.46
TiO <sub>2</sub>	0.78	0.91	0.36	0.37	0.40	0.51	0.12	0.28	1.30	0.54	1.03	0.96	0.94	1.46	1.45	1.77	1.36	0.89	0.86	2.21	0.78	0.91	0.36	0.37	0.40	0.51	0.12	0.28	1.30	0.54	1.03	0.96	0.94	1.46	1.45	1.77	1.36	0.89	0.86	2.21	0.78	0.91	0.36	0.37	0.40	0.51	0.12	0.28	1.30	0.54	1.03	0.96	0.94	1.46	1.45	1.77	1.36	0.89	0.86	2.21	0.78	0.91	0.36	0.37	0.40	0.51	0.12	0.28	1.30	0.54	1.03	0.96	0.94	1.46	1.45	1.77	1.36	0.89	0.86	2.21
Fe <sub>2</sub> O <sub>3</sub>	0.95	0.81	0.99	2.48	0.44	0.69	0.11	0.11	0.96	20.05	6.27	8.00	0.69	0.98	0.98	1.26	0.54	0.81	1.21	0.81	0.95	0.81	0.99	2.48	0.44	0.69	0.11	0.11	0.96	20.05	6.27	8.00	0.69	0.98	0.98	1.26	0.54	0.81	1.21	0.81	0.95	0.81	0.99	2.48	0.44	0.69	0.11	0.11	0.96	20.05	6.27	8.00	0.69	0.98	0.98	1.26	0.54	0.81	1.21	0.81	0.95	0.81	0.99	2.48	0.44	0.69	0.11	0.11	0.96	20.05	6.27	8.00	0.69	0.98	0.98	1.26	0.54	0.81	1.21	0.81
MnO	0.00	0.00	0.00	0.01	0.01	0.00	0.00	0.00	0.00	0.01	0.03	0.04	0.00	0.01	0.00	0.00	0.00	0.00	0.01	0.00	0.00	0.00	0.00	0.01	0.01	0.00	0.00	0.00	0.00	0.01	0.03	0.04	0.00	0.01	0.00	0.00	0.00	0.00	0.01	0.00	0.00	0.00	0.00	0.01	0.01	0.00	0.00	0.00	0.00	0.01	0.03	0.04	0.00	0.01	0.00	0.00	0.00	0.00	0.01	0.00	0.00	0.00	0.00	0.01	0.01	0.00	0.00	0.00	0.00	0.01	0.03	0.04	0.00	0.01	0.00	0.00	0.00	0.00	0.01	0.00
MgO	0.44	0.21	0.97	0.40	0.10	0.05	0.09	0.04	0.18	0.16	0.38	0.32	0.42	0.45	0.39	0.10	0.06	0.09	0.13	0.09	0.44	0.21	0.97	0.40	0.10	0.05	0.09	0.04	0.18	0.16	0.38	0.32	0.42	0.45	0.39	0.10	0.06	0.09	0.13	0.09	0.44	0.21	0.97	0.40	0.10	0.05	0.09	0.04	0.18	0.16	0.38	0.32	0.42	0.45	0.39	0.10	0.06	0.09	0.13	0.09	0.44	0.21	0.97	0.40	0.10	0.05	0.09	0.04	0.18	0.16	0.38	0.32	0.42	0.45	0.39	0.10	0.06	0.09	0.13	0.09
CaO	0.44	0.19	0.51	0.61	1.07	0.18	0.11	0.34	0.14	0.07	0.51	0.11	0.31	0.14	0.13	0.13	0.23	0.18	0.39	0.26	0.44	0.19	0.51	0.61	1.07	0.18	0.11	0.34	0.14	0.07	0.51	0.11	0.31	0.14	0.13	0.13	0.23	0.18	0.39	0.26	0.44	0.19	0.51	0.61	1.07	0.18	0.11	0.34	0.14	0.07	0.51	0.11	0.31	0.14	0.13	0.13	0.23	0.18	0.39	0.26	0.44	0.19	0.51	0.61	1.07	0.18	0.11	0.34	0.14	0.07	0.51	0.11	0.31	0.14	0.13	0.13	0.23	0.18	0.39	0.26
Na <sub>2</sub> O	0.08	0.04	0.13	0.08	0.10	0.05	0.12	0.06	0.03	0.02	0.03	0.03	0.06	0.04	0.04	0.03	0.03	0.04	0.03	0.05	0.08	0.04	0.13	0.08	0.10	0.05	0.12	0.06	0.03	0.02	0.03	0.03	0.06	0.04	0.04	0.03	0.03	0.04	0.03	0.05	0.08	0.04	0.13	0.08	0.10	0.05	0.12	0.06	0.03	0.02	0.03	0.03	0.06	0.04	0.04	0.03	0.03	0.04	0.03	0.05	0.08	0.04	0.13	0.08	0.10	0.05	0.12	0.06	0.03	0.02	0.03	0.03	0.06	0.04	0.04	0.03	0.03	0.04	0.03	0.05
K <sub>2</sub> O	1.30	0.80	3.33	0.68	0.52	0.06	0.04	0.12	0.85	0.49	1.85	1.35	1.31	2.05	1.90	0.25	0.09	0.18	0.17	0.11	1.30	0.80	3.33	0.68	0.52	0.06	0.04	0.12	0.85	0.49	1.85	1.35	1.31	2.05	1.90	0.25	0.09	0.18	0.17	0.11	1.30	0.80	3.33	0.68	0.52	0.06	0.04	0.12	0.85	0.49	1.85	1.35	1.31	2.05	1.90	0.25	0.09	0.18	0.17	0.11	1.30	0.80	3.33	0.68	0.52	0.06	0.04	0.12	0.85	0.49	1.85	1.35	1.31	2.05	1.90	0.25	0.09	0.18	0.17	0.11
P <sub>2</sub> O <sub>5</sub>	0.03	0.03	0.07	0.05	0.03	0.02	0.01	0.07	0.05	0.07	0.28	0.06	0.08	0.05	0.05	0.01	0.01	0.02	0.20	0.06	0.03	0.03	0.07	0.05	0.03	0.02	0.01	0.07	0.05	0.07	0.28	0.06	0.08	0.05	0.05	0.01	0.01	0.02	0.20	0.06	0.03	0.03	0.07	0.05	0.03	0.02	0.01	0.07	0.05	0.07	0.28	0.06	0.08	0.05	0.05	0.01	0.01	0.02	0.20	0.06	0.03	0.03	0.07	0.05	0.03	0.02	0.01	0.07	0.05	0.07	0.28	0.06	0.08	0.05	0.05	0.01	0.01	0.02	0.20	0.06
LOI	34.37	13.53	12.42	12.21	12.23	16.4	27.96	46.12	20.79	30.42	14.52	22.3	19.2	8.13	8.74	12.63	13.18	12.52	12.51	8.63	34.37	13.53	12.42	12.21	12.23	16.4	27.96	46.12	20.79	30.42	14.52	22.3	19.2	8.13	8.74	12.63	13.18	12.52	12.51	8.63	34.37	13.53	12.42	12.21	12.23	16.4	27.96	46.12	20.79	30.42	14.52	22.3	19.2	8.13	8.74	12.63	13.18	12.52	12.51	8.63	34.37	13.53	12.42	12.21	12.23	16.4	27.96	46.12	20.79	30.42	14.52	22.3	19.2	8.13	8.74	12.63	13.18	12.52	12.51	8.63
Total	99.25	99.80	99.08	99.48	99.08	99.04	99.10	99.92	99.70	95.42	98.80	99.27	99.50	99.72	99.61	99.78	99.10	99.00	99.24	99.49	99.25	99.80	99.08	99.48	99.08	99.04	99.10	99.92	99.70	95.42	98.80	99.27	99.50	99.72	99.61	99.78	99.10	99.00	99.24	99.49	99.25	99.80	99.08	99.48	99.08	99.04	99.10	99.92	99.70	95.42	98.80	99.27	99.50	99.72	99.61	99.78	99.10	99.00	99.24	99.49	99.25	99.80	99.08	99.48	99.08	99.04	99.10	99.92	99.70	95.42	98.80	99.27	99.50	99.72	99.61	99.78	99.10	99.00	99.24	99.49
CIA	93.86	97.21	87.54	96.88	97.20	99.39	98.97	98.66	97.03	97.36	95.28	94.50	95.47	93.20	93.70	99.01	99.44	98.99	99.11	98.69	93.86	97.21	87.54	96.88	97.20	99.39	98.97	98.66	97.03	97.36	95.28	94.50	95.47	93.20	93.70	99.01	99.44	98.99	99.11	98.69	93.86	97.21	87.54	96.88	97.20	99.39	98.97	98.66	97.03	97.36	95.28	94.50	95.47	93.20	93.70	99.01	99.44	98.99	99.11	98.69	93.86	97.21	87.54	96.88	97.20	99.39	98.97	98.66	97.03	97.36	95.28	94.50	95.47	93.20	93.70	99.01	99.44	98.99	99.11	98.69

CIA =  $[\text{Al}_2\text{O}_3 / (\text{Al}_2\text{O}_3 + \text{CaO}^* + \text{Na}_2\text{O} + \text{K}_2\text{O})] \times 100$  (CaO\* represents the amount in silicates only) (Nesbitt and Young 1982), LOI: loss on ignition at 900°C.

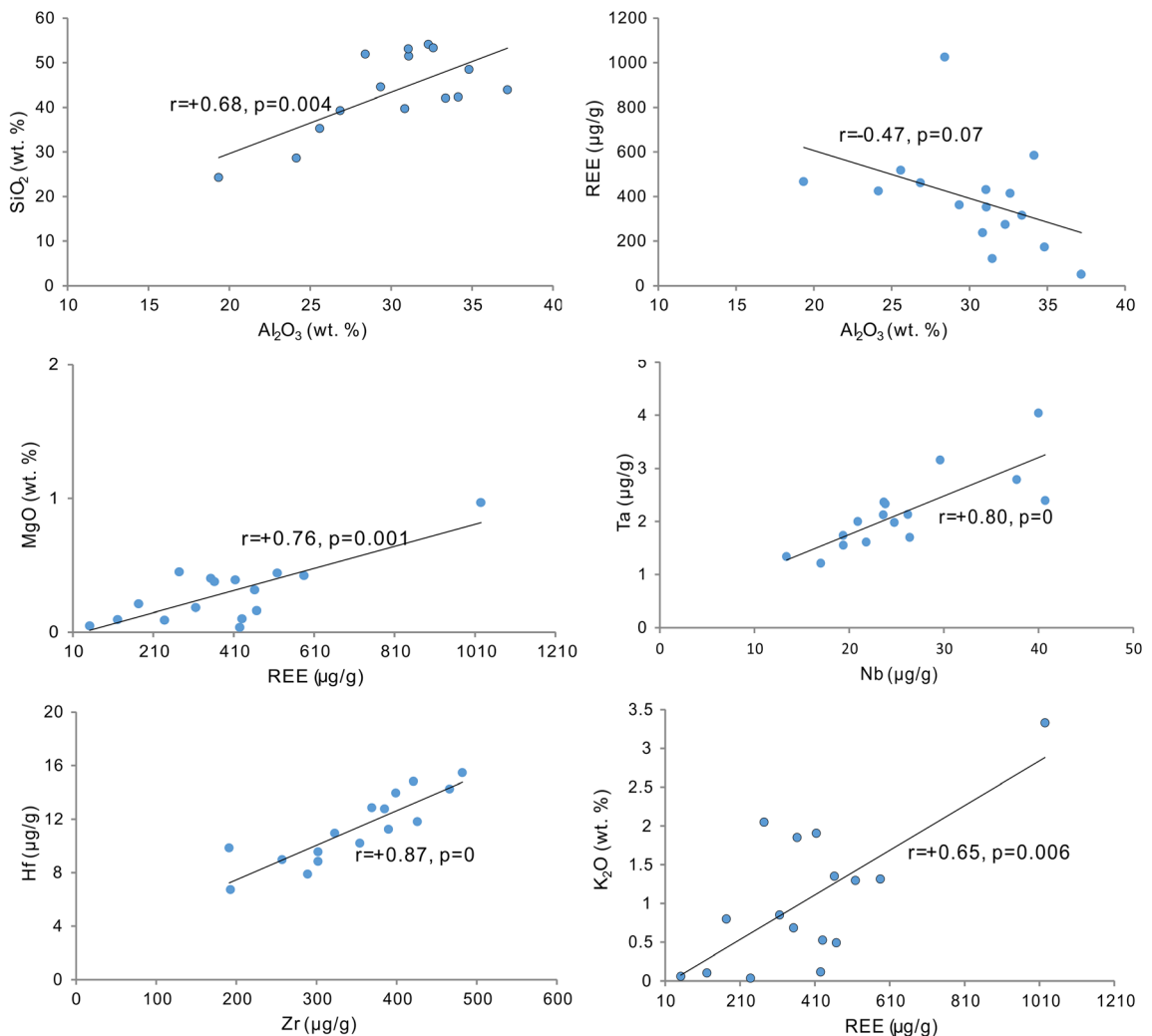


**Fig. 7** Relational diagram for feature elements of the analyzed claystones (all correlations shown are for the kaolinitic claystone samples);  $r$  is Pearson's correlation coefficient

samples because of their strong resistance to weathering (Panahi et al. 2000). Nb, Ta, Th, and U concentrations were significantly higher in cryptocrystalline kaolinitic claystones than in tonsteins (Fig. 9; Table 5), which is consistent with tonsteins generally having smaller HFSE contents than other types of claystones (Zielinski 1985). In the study samples, only Nb showed covariation with  $\text{Al}_2\text{O}_3$  but other HFSEs exhibited significant correlations with MnO and CaO (Table 4), indicating that these elements were probably hosted in detrital minerals. A strong correlation between Zr and Hf ( $r = +0.87$ ,  $p < 0.01$ ; Fig. 7) indicated that both elements reside mostly in zircon. A strong correlation exists between Nb and Ta ( $r = +0.80$ ,  $p < 0.01$ ; Fig. 7) owing to their close geochemical affinity. The correlation between Th and  $\text{Al}_2\text{O}_3$  is not strong (Table 4), indicating that Th may be hosted in secondary minerals or organic matter. U and  $\text{Al}_2\text{O}_3$  showed a negative linear correlation (Table 4), suggesting that U was adsorbed on clay minerals (Taboada et al. 2006) and then lost during the process of kaolinization.

The large ion lithophile elements (LILEs), including Rb, Cs, Sr, and Ba, were almost entirely depleted in the samples, but the tonstein samples had lost a larger fraction of the LILEs (Fig. 9). Small amounts of LILE are due to these elements having been removed preferentially from the parent rock during kaolinization and to the small cation exchange capacity (CEC) of the neoformed kaolinite (Galán et al. 2016; Lopez et al. 2005). Other trace elements including Li, Ga, Cd, In, Sb, Pb, and Bi were enriched in the cryptocrystalline kaolinitic claystones, but only Li and Ga were enriched in the tonsteins. Statistical analysis showed that those elements which do not show a positive correlation with  $\text{Al}_2\text{O}_3$  (Table 4) may be present in secondary minerals (e.g. pyrite, anatase, or zircon) or organic matter.

#### Rare Earth Elements

The total REE contents ( $\Sigma\text{REE}$ ) of the claystones in the study units ranged between 29.2 and 934 ppm with an average

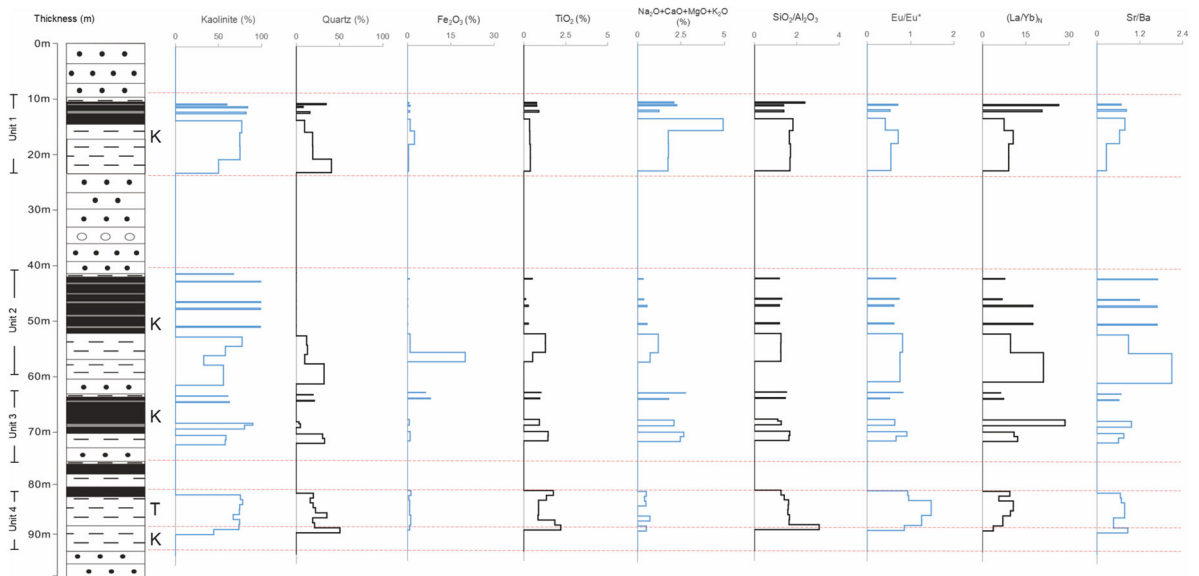


**Fig. 8** Geochemical variations along the section studied in the Nanyangpo mine. The left column shows lithology. The red dotted lines separate the claystone from the sandstone; K: cryptocrystalline kaolinitic claystone; T: tonstein

of 275 ppm. The ratio of total light rare earth elements ( $\Sigma$ LREE) to total heavy rare earth elements ( $\Sigma$ HREE) ranged between 6.4 and 26.8 with an average of 14.8 and indicates the fractionation of light and heavy rare earths, i.e. enrichment of LREE and depletion of HREE.

The REEs were normalized to chondrite values (Fig. 10) (McDonough and Sun 1995). Based on their distribution patterns, the main difference between cryptocrystalline kaolinitic claystone and tonstein samples are with regard to their Eu anomalies. The cryptocrystalline kaolinitic claystone samples exhibit pronounced negative Eu anomalies, having  $\text{Eu}/\text{Eu}^*$  of 0.42–0.92 with an average of 0.70.  $\text{Ce}/\text{Ce}^*$  values vary from 0.69 to 1.29 with an average of 0.90, revealing no anomaly or weak negative Ce anomalies. These features are consistent with a sedimentary origin of these claystones (Wang et al. 2013). The REE distribution patterns of the tonstein samples were characterized by weak negative to weak positive Eu anomalies ( $\text{Eu}/\text{Eu}^*$  of 0.94 to 1.48 with an average of 1.16) and weak negative Ce anomalies ( $\text{Ce}/\text{Ce}^*$  of 0.74 to 0.99 with an average of 0.82).

The  $\Sigma$ REE contents of the study units may have been affected by remobilization during diagenesis. The  $\Sigma$ REE in the study area show a negative correlation with  $\text{Al}_2\text{O}_3$  ( $r = -0.47$ ,  $p = 0.07$ ) but a positive correlation with  $\text{MgO}$  ( $r = +0.76$ ,  $p < 0.01$ ) and a weak covariation with  $\text{K}_2\text{O}$  ( $r = +0.65$ ,  $p < 0.01$ ) (Fig. 7). The REEs may be mobilized and lost during alteration of the parent rocks.

## DISCUSSION

### *Salinity, Redox, and Weathering Conditions of the Depositional System*

The sedimentary environment of the Upper Carboniferous–Lower Permian Taiyuan Formation in the Datong Basin was a mixed marine–continental transitional facies (Wang and Guo

2020; Hou et al. 2019; Liu et al. 2020a). Salinity and redox conditions in the depositional system may be assessed using geochemical proxies. For example, Wei and Algeo (2020) showed that, without the influence of carbonate, the ratio of  $\text{Sr}/\text{Ba}$  increases gradually during the transition from continental environments to marine environments. In the present study units, almost no carbonate minerals are present and the amount of  $\text{CaO}$  is very small, so  $\text{Sr}/\text{Ba}$  ratios were used to help infer the salinity of the depositional environment. The ratios of  $\text{Sr}/\text{Ba}$  in the claystones of Units 1, 2, and 4 are 0.27–0.83, 0.61–0.97, and 0.47–0.87, respectively (Fig. 8), suggesting a transitional environment with variation from brackish to marine conditions. Unit 3 yielded greater  $\text{Sr}/\text{Ba}$  ratios (0.89–2.10; Fig. 8) which are potentially consistent with fully marine sedimentation (Burton and Price 1990; Martinez-Ruiz et al. 2015; Wei et al. 2018).

Redox conditions of the depositional system can be evaluated on the basis of trace-metal concentrations and enrichment factors (EFs) (Algeo and Liu 2020).  $\text{U}/\text{Th}$  ratios of 0.11–1.09 indicate oxic to anoxic conditions. The EFs of Mo and V are low, and  $\text{U}_{\text{EF}} > \text{Mo}_{\text{EF}}$ , which are suggestive of dominantly suboxic conditions (Algeo and Tribovillard 2009; Tribovillard et al. 2006).

The chemical index of alteration (CIA) (Nesbitt and Young 1982) was calculated to evaluate the degree of chemical weathering of detrital material in the study samples. This index was calculated using molecular proportions of the following oxides:  $\text{CIA} = [\text{Al}_2\text{O}_3 / (\text{Al}_2\text{O}_3 + \text{CaO}^* + \text{Na}_2\text{O} + \text{K}_2\text{O})] \times 100$ , where  $\text{CaO}^*$  represents the amount of  $\text{CaO}$  associated with the silicate fraction of the rock. The CIA values of the study samples were in the range 87.5–99.4; such high values are indicative of intense chemical weathering (Eggleton et al. 1987). The kaolinite formed in an open acidic and hydrologic system in which Na, Ca, and K were leached out (Dalai et al.

**Table 3** Trace-element compositions (ppm) of claystone samples in the study area, determined by ICP-MS analysis

Trace elements (ppm)	Section I samples							Section II samples							Section III samples							Section IV samples						
	NP-7	NP-8	NP-9	NP-10	NP-11	NP-17	NP-18	NP-19	NP-21	NP-23	NP-25	NP-26	NP-27	NP-29	NP-30	NP-32	NP-33	NP-34	NP-37	NP-39								
Li	68.60	70.21	24.70	26.30	82.10	126.00	93.40	79.90	145.20	71.90	114.30	160.60	247.00	121.90	126.00	234.00	107.00	83.40	71.10	88.10								
Be	2.66	2.58	2.37	1.40	3.38	0.36	0.39	1.09	2.62	1.96	2.37	2.51	1.28	1.99	2.10	1.19	1.08	1.42	1.06	0.61								
Sc	7.67	10.05	9.95	15.07	8.25	3.50	5.93	3.41	22.89	16.21	24.31	24.45	10.00	21.27	21.90	17.90	21.70	23.40	23.20	15.00								
V	53.80	62.52	43.30	19.33	22.40	7.09	28.00	15.60	150.94	150.08	207.85	128.47	76.60	96.88	99.70	91.70	151.00	114.00	111.00	84.50								
Cr	35.90	23.34	12.10	7.94	7.79	2.79	3.65	4.68	105.39	57.19	100.73	60.76	47.50	76.27	98.20	43.00	93.60	102.00	88.10	71.70								
Co	3.78	4.66	2.61	1.40	3.18	0.63	0.67	0.72	7.22	15.71	18.75	16.39	6.99	5.27	7.74	3.10	2.14	6.12	11.90	4.32								
Ni	18.80	14.40	6.94	4.27	4.44	1.08	3.73	4.02	26.74	75.61	54.36	71.92	29.00	18.04	21.90	5.88	6.63	10.10	12.30	9.24								
Cu	11.10	7.72	8.35	6.01	6.80	7.18	79.50	77.90	20.31	18.40	17.34	27.89	86.30	16.49	22.10	10.10	7.74	9.53	11.10	12.50								
Zn	64.80	56.70	50.30	49.50	79.60	16.10	26.70	24.00	75.40	57.90	50.80	89.50	54.40	65.60	78.30	76.50	50.80	125.00	255.00	60.80								
Ga	34.80	31.30	37.60	33.60	42.40	40.60	26.90	20.70	34.80	26.00	34.40	33.40	29.50	33.20	37.70	46.20	40.40	39.70	39.50	41.90								
Rb	101.00	94.34	158.00	31.47	17.40	5.18	5.37	3.90	24.47	18.55	19.25	13.41	53.70	56.59	72.60	8.21	2.83	5.28	5.38	5.14								
Sr	74.00	60.60	92.80	59.60	51.20	38.60	41.90	41.90	90.00	240.60	74.93	83.80	193.00	97.00	85.90	41.60	27.30	65.90	71.60	37.10								
Y	20.90	22.91	132.00	28.26	32.20	23.33	25.30	24.30	21.40	19.30	23.30	25.60	18.30	13.00	28.50	15.50	9.26	44.70	44.90	18.80								
Mo	0.88	1.23	2.14	3.29	1.34	1.70	1.42	0.97	1.57	20.47	1.14	1.84	0.80	1.20	0.38	0.51	0.54	0.27	0.38	1.17								
Cd	0.12	2.88	0.13	2.52	0.24	0.05	0.12	0.12	0.17	0.33	0.30	3.54	0.07	0.11	0.18	0.13	0.07	0.14	0.23	0.11								
In	0.11	0.15	0.10	0.14	0.08	0.03	0.09	0.06	0.09	0.10	0.17	0.21	0.10	0.09	0.08	0.13	0.08	0.06	0.07	0.10								
Sb	0.34	0.32	0.27	0.31	0.40	0.09	0.18	0.25	1.09	2.35	1.05	1.42	0.25	0.18	0.16	0.07	0.07	0.05	0.06	0.23								
Cs	20.10	0.40	13.40	0.94	1.22	0.94	0.35	0.39	1.86	1.25	0.69	0.85	6.90	6.61	10.40	0.98	0.27	0.28	0.25	1.14								
Ba	109.00	73.30	118.00	93.20	191.00	22.70	35.20	24.80	101.51	114.66	109.44	134.55	198.00	127.93	171.00	62.70	39.40	85.00	152.00	42.60								
La	120.00	25.70	186.00	62.80	59.90	5.90	27.20	89.20	48.10	97.10	50.30	76.70	116.00	35.40	72.00	27.20	7.80	91.30	55.80	15.30								
Ce	165.00	37.10	378.00	112.40	106.00	12.80	89.10	177.00	92.00	164.70	112.70	150.71	167.00	59.00	109.00	62.90	14.00	145.00	87.30	29.20								
Pr	16.90	5.46	44.30	12.90	11.40	1.41	12.00	20.30	10.85	16.27	13.12	14.67	17.10	6.88	12.90	7.01	1.84	17.60	10.40	3.81								
Nd	61.10	20.75	182.00	44.01	37.90	5.04	48.60	77.30	36.47	46.64	41.68	45.28	57.10	24.10	45.80	35.80	8.24	75.40	47.30	16.50								
Sm	8.90	2.69	34.70	7.05	6.67	0.78	9.65	12.80	7.24	7.46	9.02	8.44	7.28	4.63	7.11	5.92	1.81	15.10	8.82	3.54								
Eu	1.96	0.41	4.56	1.56	1.18	0.17	1.94	2.47	1.90	1.90	2.61	1.61	1.56	1.31	1.51	1.62	0.50	6.90	3.61	0.95								
Gd	8.09	2.10	31.20	6.26	6.38	0.79	6.66	11.70	6.97	7.85	10.28	10.49	7.59	4.11	6.67	4.67	1.41	13.40	8.77	3.24								
Tb	1.26	0.35	5.39	1.12	1.15	0.15	1.22	1.77	0.90	0.81	1.32	1.85	1.04	0.52	1.19	0.90	0.31	2.34	1.69	0.70								
Dy	5.58	1.83	26.80	7.82	7.28	0.92	5.54	7.15	6.49	5.88	9.76	11.89	4.97	3.58	5.99	4.02	1.66	10.90	9.31	4.02								
Ho	0.85	0.26	5.25	1.43	1.33	0.17	0.98	1.08	1.03	0.86	1.72	2.63	0.80	0.61	1.16	0.74	0.31	1.96	1.87	0.83								
Er	2.69	0.78	14.90	4.37	3.80	0.44	2.77	3.21	3.14	3.11	6.00	8.56	2.60	2.09	3.56	1.98	0.92	5.78	4.79	2.31								
Tm	0.44	0.13	2.59	0.74	0.70	0.08	0.44	0.50	0.45	0.43	1.01	1.47	0.42	0.33	0.65	0.32	0.14	0.96	0.85	0.42								

**Table 3** (continued)

Trace elements (ppm)	Section I samples				Section II samples				Section III samples				Section IV samples							
	NP-7	NP-8	NP-9	NP-10	NP-11	NP-17	NP-18	NP-19	NP-21	NP-23	NP-25	NP-26	NP-27	NP-29	NP-30	NP-32	NP-33	NP-34	NP-37	NP-39
Yb	3.06	0.84	16.60	4.59	4.42	0.51	2.68	3.44	3.32	3.09	5.38	6.99	2.73	2.17	3.97	1.92	0.92	5.73	5.29	2.71
Lu	0.38	0.11	1.93	0.49	0.47	0.06	0.34	0.43	0.37	0.40	0.66	0.81	0.35	0.31	0.59	0.23	0.13	0.72	0.67	0.38
W	2.97	2.96	1.58	4.89	2.88	2.90	2.37	2.14	3.86	3.12	2.65	2.98	4.35	4.96	5.41	2.28	1.88	3.10	1.88	10.00
Pb	66.20	58.91	69.70	62.67	96.20	6.99	15.60	13.80	25.59	109.63	19.68	26.70	45.60	25.20	30.50	20.00	13.40	7.88	10.30	37.40
Tl	0.80	0.17	0.35	0.71	0.16	0.06	0.04	0.03	0.04	0.35	0.95	0.77	0.24	0.48	0.35	0.05	0.02	0.03	0.04	0.02
Bi	0.61	0.31	0.59	0.23	0.57	0.17	0.22	0.38	0.95	0.61	0.49	0.48	0.83	0.44	0.35	0.18	0.06	0.04	0.04	0.91
Th	26.30	24.80	56.60	31.46	45.80	10.30	13.20	29.00	22.73	14.76	24.91	21.99	26.70	15.42	21.00	8.06	4.58	4.51	4.19	16.70
U	4.91	4.94	15.20	8.66	15.50	3.49	2.23	3.18	2.75	16.10	6.07	7.41	3.80	3.80	4.93	2.57	1.40	1.20	1.18	4.86
Nb	21.80	24.77	29.60	23.67	40.00	37.70	17.00	20.90	23.59	13.38	19.38	23.83	26.20	19.37	26.40	18.20	14.00	10.90	10.60	40.70
Ta	1.61	1.98	3.16	2.37	4.04	2.79	1.21	2.00	2.12	1.34	1.55	2.33	2.13	1.73	1.70	1.10	0.73	0.64	0.88	2.40
Zr	289.00	192.70	385.00	322.80	302.00	191.00	426.00	369.00	354.00	302.00	399.00	482.00	257.00	389.80	466.00	533.00	320.00	223.00	317.00	421.00
Hf	7.88	6.73	12.77	10.95	8.84	9.85	11.82	12.86	10.21	9.57	13.95	15.47	8.97	11.25	14.26	16.44	9.08	8.14	8.50	14.82
ΣREE	396.22	98.52	934.22	267.54	248.58	29.21	209.11	408.36	219.21	356.51	265.56	342.10	386.54	145.05	272.10	155.23	39.99	393.08	246.47	83.91
ΣLREE	373.86	92.12	829.56	240.73	223.05	26.10	188.49	379.07	196.56	334.08	229.43	297.42	366.04	131.32	248.32	140.45	34.19	351.30	213.23	69.30
ΣHREE	22.36	6.40	104.66	26.81	25.53	3.11	20.62	29.29	22.66	22.43	36.13	44.69	20.50	13.73	23.78	14.78	5.80	41.78	33.24	14.61
ΣLREE/ΣHREE	16.72	14.39	7.93	8.98	8.74	8.39	9.14	12.94	8.68	14.89	6.35	6.66	17.85	9.56	10.44	9.50	5.89	8.41	6.42	4.74
Eu/Eu*	0.71	0.53	0.42	0.72	0.55	0.66	0.74	0.62	0.82	0.76	0.83	0.52	0.64	0.92	0.67	0.94	0.96	1.48	1.26	0.86
Ce/Ce*	0.70	0.69	0.93	0.77	0.88	1.03	1.29	0.93	0.92	0.87	1.06	0.98	0.74	0.82	0.75	0.99	0.81	0.75	0.74	0.86
(La/Sm) <sub>N</sub>	8.48	6.01	3.37	6.50	5.65	4.73	1.77	4.38	4.18	8.19	3.51	5.71	10.02	4.81	6.37	2.89	2.72	3.80	3.98	2.72
(La/Yb) <sub>N</sub>	26.44	20.64	7.55	10.70	9.14	7.75	6.84	17.48	9.76	21.18	6.31	7.39	28.65	10.99	12.23	9.55	5.74	10.74	7.11	3.81
(La/Lu) <sub>N</sub>	32.80	24.29	10.01	15.44	13.24	10.14	8.31	21.55	13.50	25.21	7.92	9.83	34.43	11.85	12.68	12.28	6.26	13.17	8.65	4.18
(Gd/Yb) <sub>N</sub>	2.13	2.02	1.52	1.10	1.16	1.25	2.01	2.74	1.69	2.05	1.54	1.21	2.24	1.53	1.36	1.96	1.24	1.89	1.34	0.96

Eu/Eu\* =  $Eu_N / (Sm_N \times Gd_N)^{1/2}$  and Ce/Ce\* =  $3Ce_N / (2La_N + Nd_N)$  (Mongelli 1997).

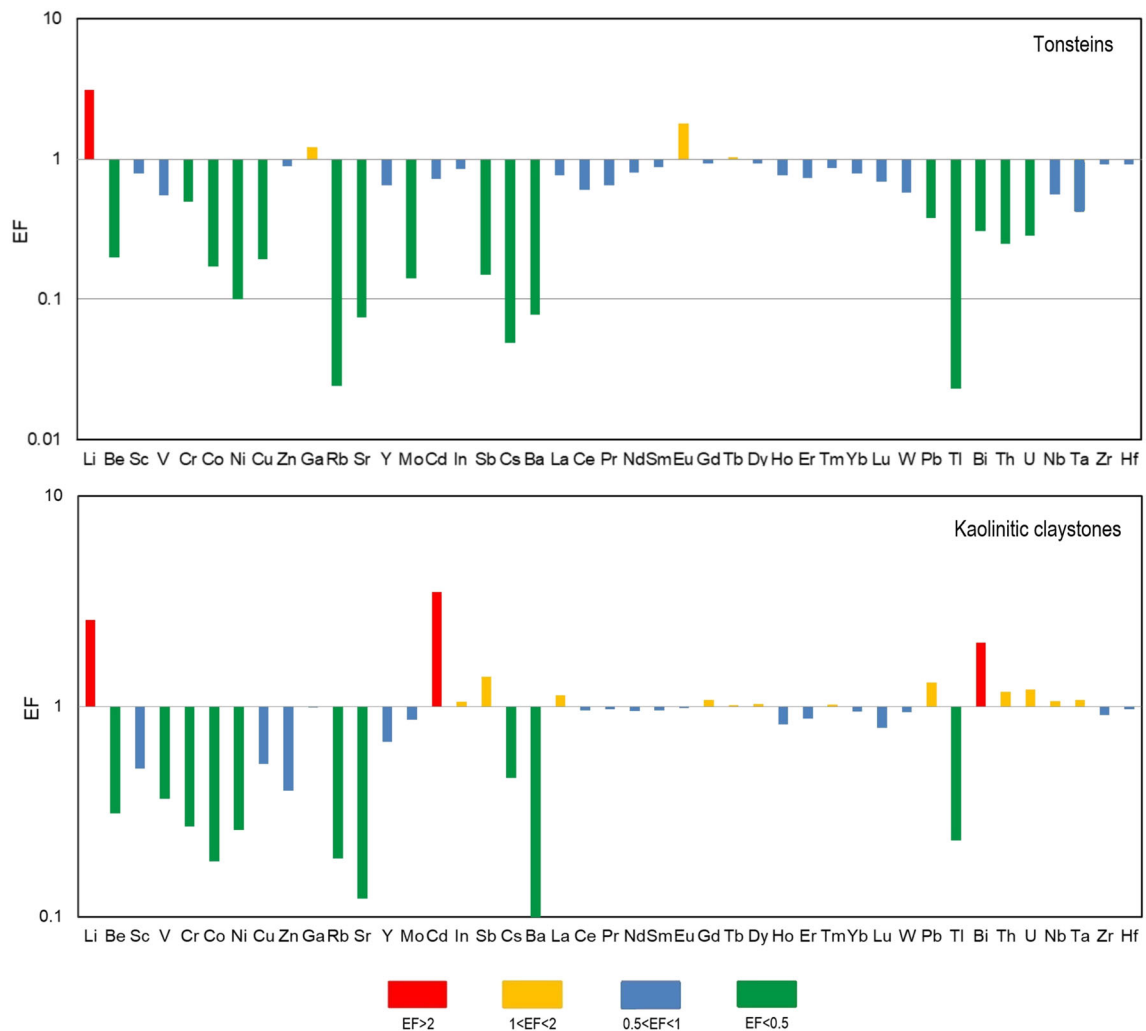


**Fig. 9** Enrichment Factors (EFs) of trace elements in cryptocrystalline kaolinitic claystones and tonsteins in the Nanyangpo mine. UCC data are from Taylor and McLennan (1985) and McLennan (2001)

2004; Erkoyun et al. 2017). In addition, the CIA can also help to analyze paleoclimate conditions during weathering. The strong chemical weathering ( $CIA = 80\text{--}100$ ) implies a warm and humid paleoclimate in the source area (Nesbitt and Young 1982). Collectively, the foregoing analyses demonstrate that claystones in the Datong Coalfield were deposited in an acidic and anoxic transitional-marine environment.

#### *Mineral Composition and Structure of Claystone*

Textural and morphological images show that the claystones of the Nanyangpo mine contain pseudo-hexagonal platy and vermicular kaolinite crystals within a cryptocrystalline kaolinitic matrix accompanied by illite, quartz, and secondary diagenetic minerals. Similar compositions were reported by Baioumy and Gharai (2008), Arbusov et al. (2016), and Tauler et al. (2019) for kaolinite-rich clay deposits from southern Iberia, kaolin deposits from Huíla (Colombia), and tonstein deposits from the Irkutsk Coal Basin, respectively. The Hinkley index shows that both ordered and disordered forms

of kaolinite are present in the study samples (Table 1). The well-ordered ( $HI > 1$ ) vermiform and plate-like morphologies suggest in situ formation (Erkoyun et al. 2019; Kadir and Erkoyun 2013). These types of kaolinite can be generated by alteration of feldspars and micas in aluminosilicate clastics or volcanic ash (Erkoyun et al. 2017), and they are present in both the cryptocrystalline kaolinitic claystones and tonsteins. In contrast, the bulk of kaolinite in the study samples is disordered and occurs as a cryptocrystalline matrix, which may have formed through recrystallization of silica-alumina colloids produced by weathering in an acidic peat swamp environment (Kadir and Akbulut 2009). The action of organic acids in a swamp environment can alter terrigenous fine-grained clays and volcanic glass to a cryptocrystalline kaolinitic matrix (Liu et al. 2020b; Kadir et al. 2011). The weakly recrystallized vitric fragments and the presence of tuffaceous clastic grains in the tonsteins of the study units, as seen in the polarizing microscope images (Fig. 4), may represent air-fall volcanic ash deposited in a non-marine, coal-forming

**Table 4** Pearson correlation coefficient of major oxides, trace elements, and some element groups of investigated samples

	Al <sub>2</sub> O <sub>3</sub>	SiO <sub>2</sub>	TiO <sub>2</sub>	Fe <sub>2</sub> O <sub>3</sub>	MnO	MgO	CaO	Na <sub>2</sub> O	K <sub>2</sub> O	P <sub>2</sub> O <sub>5</sub>	Li	Be	Sc	V	Cr	Co	Ni	Cu	Zn	Ga	
Al <sub>2</sub> O <sub>3</sub>	<b>1</b>	0.68	0.28	-0.68	-0.25	-0.06	-0.01	0.06	-0.02	-0.19	0.35	-0.19	-0.04	-0.23	0.02	-0.37	-0.52	-0.09	-0.08	0.50	
SiO <sub>2</sub>		<b>1</b>	0.44	-0.55	-0.05	0.31	0.32	0.24	0.34	-0.05	-0.08	0.10	0.21	-0.14	0.12	-0.26	-0.46	-0.44	0.28	0.73	
TiO <sub>2</sub>			<b>1</b>	-0.09	0.10	-0.02	-0.32	-0.55	0.14	0.34	0.03	0.03	0.59	0.50	0.77	0.28	0.16	-0.25	0.50	0.41	
Fe <sub>2</sub> O <sub>3</sub>				<b>1</b>	0.42	-0.07	-0.25	-0.46	-0.03	0.29	-0.06	0.15	0.36	0.56	0.24	0.73	0.84	-0.15	0.18	-0.30	
MnO					<b>1</b>	0.12	0.05	-0.33	0.23	0.60	0.19	0.27	0.60	0.55	0.32	0.75	0.68	-0.14	0.34	0.03	
MgO						<b>1</b>	0.16	0.36	0.93	0.21	-0.15	0.35	0.22	0.10	0.09	0.09	0.05	-0.22	0.23	0.17	
CaO							<b>1</b>	0.51	0.09	0.16	-0.34	0.40	-0.25	-0.32	-0.36	-0.22	-0.33	-0.24	0.11	0.37	
Na <sub>2</sub> O								<b>1</b>	0.15	-0.26	-0.39	-0.12	-0.57	-0.65	-0.65	-0.62	-0.62	0.18	-0.31	0.10	
K <sub>2</sub> O									<b>1</b>	0.33	-0.01	0.49	0.41	0.31	0.32	0.27	0.18	-0.24	0.37	0.20	
P <sub>2</sub> O <sub>5</sub>										<b>1</b>	0.12	0.15	0.45	0.67	0.46	0.65	0.46	-0.01	-0.01	-0.07	
Li											<b>1</b>	-0.10	0.26	0.33	0.43	0.33	0.32	0.48	0.20	-0.06	
Be												<b>1</b>	0.39	0.28	0.39	0.33	0.33	-0.46	0.75	0.22	
Sc													<b>1</b>	0.84	0.87	0.74	0.64	-0.31	0.68	0.16	
V														<b>1</b>	0.88	0.90	0.81	-0.14	0.48	-0.04	
Cr															<b>1</b>	0.67	0.55	-0.16	0.58	0.16	
Co																<b>1</b>	0.95	-0.12	0.48	-0.08	
Ni																	<b>1</b>	-0.04	0.44	-0.24	
Cu																		<b>1</b>	-0.37	-0.69	
Zn																			<b>1</b>	0.36	
Ga																				<b>1</b>	
Rb																					
Sr																					
Y																					
Mo																					
Cd																					
In																					
Sb																					
Cs																					
Ba																					
W																					
Pb																					
Tl																					
Bi																					
Th																					
U																					
Nb																					



Table 4 (continued)

	Al <sub>2</sub> O <sub>3</sub>	SiO <sub>2</sub>	TiO <sub>2</sub>	Fe <sub>2</sub> O <sub>3</sub>	MnO	MgO	CaO	Na <sub>2</sub> O	K <sub>2</sub> O	P <sub>2</sub> O <sub>5</sub>	Li	Be	Sc	V	Cr	Co	Ni	Cu	Zn	Ga	
Ta																					
Zr																					
Hf																					
REE																					
Al <sub>2</sub> O <sub>3</sub>	0.03	-0.40	-0.10	-0.64	0.01	-0.19	-0.63	-0.13	-0.09	0.26	-0.43	-0.31	-0.11	-0.12	-0.48	0.51	0.28	-0.28	-0.16	-0.47	
SiO <sub>2</sub>	0.27	-0.42	0.24	-0.55	0.06	0.02	-0.58	0.07	0.17	0.48	-0.07	-0.02	0.00	0.27	0.00	0.59	0.46	0.14	0.17	-0.15	
TiO <sub>2</sub>	-0.03	0.00	-0.31	-0.20	-0.07	0.13	-0.03	0.07	0.11	0.81	-0.23	0.01	0.53	-0.34	-0.33	0.25	-0.15	0.31	0.33	-0.38	
Fe <sub>2</sub> O <sub>3</sub>	-0.21	0.69	-0.12	0.91	0.17	0.31	0.92	-0.21	0.20	-0.13	0.46	0.32	0.08	-0.23	0.52	-0.46	-0.32	0.05	0.06	0.10	
MnO	-0.26	0.04	-0.11	0.02	0.50	0.77	0.47	-0.25	0.39	-0.10	-0.13	0.72	-0.04	-0.03	0.13	-0.19	-0.05	0.42	0.50	0.02	
MgO	0.83	0.22	0.73	-0.12	0.02	0.29	-0.11	0.68	0.43	-0.17	0.21	0.49	0.10	0.59	0.32	-0.12	0.10	0.18	0.12	0.76	
CaO	0.11	-0.26	0.28	-0.22	-0.07	-0.01	-0.24	0.09	0.33	-0.15	0.45	0.18	0.04	0.75	0.50	0.43	0.69	-0.17	-0.18	0.25	
Na <sub>2</sub> O	0.34	-0.30	0.60	-0.29	-0.22	-0.23	-0.53	0.31	-0.04	-0.27	0.17	-0.13	-0.19	0.58	0.23	0.19	0.36	0.03	-0.08	0.49	
K <sub>2</sub> O	0.76	0.22	0.63	-0.16	-0.03	0.30	-0.03	0.62	0.55	-0.19	0.09	0.50	0.12	0.51	0.26	-0.14	0.06	0.30	0.22	0.65	
P <sub>2</sub> O <sub>5</sub>	-0.10	0.16	0.01	0.03	-0.10	0.40	0.32	-0.13	0.26	-0.09	-0.14	0.53	0.14	0.08	0.06	-0.26	-0.22	0.22	0.36	0.14	
Li	-0.27	0.34	-0.43	-0.21	-0.10	0.04	0.05	-0.08	0.40	0.13	-0.41	-0.08	0.33	-0.37	-0.46	0.01	-0.14	0.02	0.05	-0.25	
Be	0.42	0.16	0.19	0.02	0.23	0.40	0.33	0.29	0.62	-0.31	0.50	0.41	0.25	0.52	0.47	-0.07	0.26	0.01	-0.23	0.29	
Sc	-0.06	0.24	-0.16	0.09	0.26	0.56	0.48	-0.08	0.49	0.30	-0.11	0.50	0.29	-0.17	0.01	-0.27	-0.26	0.56	0.47	-0.09	
V	-0.11	0.45	-0.21	0.30	0.03	0.48	0.69	-0.09	0.39	0.11	-0.04	0.42	0.44	-0.26	0.02	-0.40	-0.43	0.35	0.30	-0.05	
Cr	-0.06	0.29	-0.29	0.03	-0.12	0.27	0.38	0.07	0.39	0.41	-0.20	0.27	0.51	-0.32	-0.21	-0.20	-0.39	0.45	0.37	-0.18	
Co	-0.15	0.52	-0.19	0.41	0.23	0.62	0.79	-0.14	0.50	-0.04	0.10	0.56	0.26	-0.19	0.22	-0.38	-0.33	0.31	0.31	0.03	
Ni	-0.16	0.64	-0.21	0.57	0.28	0.58	0.89	-0.12	0.44	-0.11	0.18	0.50	0.25	-0.25	0.25	-0.49	-0.38	0.25	0.21	0.08	
Cu	-0.28	0.17	-0.19	-0.12	-0.22	-0.15	-0.13	-0.14	-0.06	-0.17	-0.37	-0.31	0.01	-0.17	-0.42	-0.34	-0.35	0.15	0.10	0.10	
Zn	0.19	0.22	-0.06	0.00	0.30	0.47	0.33	0.22	0.71	0.26	0.35	0.34	0.47	0.19	0.28	0.06	0.15	0.35	0.10	0.05	
Ga	0.15	-0.35	0.21	-0.33	-0.08	-0.08	-0.27	0.19	0.22	0.39	0.09	0.04	0.18	0.21	0.19	0.79	0.62	-0.01	0.09	-0.15	
Rb	<b>I</b>	0.13	0.67	-0.15	0.01	0.10	-0.26	0.77	0.20	-0.21	0.33	0.21	0.05	0.56	0.24	-0.04	0.09	-0.13	-0.24	0.62	
Sr	<b>I</b>	<b>I</b>	-0.03	0.72	-0.11	0.08	0.62	0.14	0.47	-0.07	0.48	0.13	0.37	-0.08	0.37	-0.44	-0.29	-0.14	-0.23	0.29	
Y			<b>I</b>	-0.06	-0.08	0.00	-0.14	0.38	0.09	-0.33	0.24	0.01	0.02	0.76	0.52	0.18	0.44	0.13	0.17	0.83	
Mo				<b>I</b>	-0.02	-0.02	0.78	-0.17	0.03	-0.10	0.60	0.03	0.07	-0.19	0.57	-0.40	-0.26	-0.14	-0.17	0.11	
Cd				<b>I</b>	0.77	<b>I</b>	0.21	-0.31	0.01	-0.07	0.08	0.36	-0.31	0.03	0.06	-0.11	0.04	0.00	0.03	-0.11	
In				<b>I</b>	0.39	<b>I</b>	0.39	-0.10	0.30	-0.04	0.08	0.69	0.04	0.11	0.10	-0.30	-0.16	0.29	0.25	0.12	
Sb				<b>I</b>	<b>I</b>	<b>I</b>	<b>I</b>	-0.26	0.25	-0.18	0.37	0.29	0.27	-0.17	0.44	-0.46	-0.26	0.11	0.06	0.09	
Cs				<b>I</b>	0.32	<b>I</b>	0.32	0.19	0.32	-0.07	0.21	0.32	0.19	0.32	0.06	-0.05	-0.06	0.03	-0.14	0.53	
Ba				<b>I</b>	-0.07	<b>I</b>	0.34	0.47	0.31	-0.07	0.34	0.47	0.31	0.36	0.40	-0.03	0.21	0.24	0.07	0.32	
W				<b>I</b>	-0.09	<b>I</b>	-0.09	-0.16	0.40	-0.33	-0.23	-0.33	0.40	-0.33	-0.23	0.40	-0.03	0.23	0.30	-0.44	
Pb				<b>I</b>	0.11	0.22	0.47	0.84	0.02	0.28	-0.31	-0.47	0.84	0.02	0.28	-0.31	-0.47	0.84	0.02	0.28	

Table 4 (continued)

	Al <sub>2</sub> O <sub>3</sub>	SiO <sub>2</sub>	TiO <sub>2</sub>	Fe <sub>2</sub> O <sub>3</sub>	MnO	MgO	CaO	Na <sub>2</sub> O	K <sub>2</sub> O	P <sub>2</sub> O <sub>5</sub>	Li	Be	Sc	V	Cr	Co	Ni	Cu	Zn	Ga	
Ti																					0.22
Bi																					0.18
Th																					0.02
U																					-0.06
Nb																					-0.08
Ta																					0.04
Zr																					-0.07
Hf																					0.87
REE																					0.15

environment (Bohor and Triplehorn 1993; Liu et al. 2019). Minor amounts of illite were detected by XRD, but no textural evidence was found for illite authigenesis in any of the samples. Small proportions of detrital sediment are common in claystones (Spears 2012), and this is the likely origin of illite in the study samples. Detrital illite represents an intermediate product in the mica/K-feldspar-to-kaolinite transformation series in the source area (Bauluz et al. 2008).

Cathodoluminescence images revealed multiple types of quartz in the claystones, including terrigenous clastic quartz, volcanic clastic quartz, and authigenic quartz. The terrigenous clastic quartz exhibited good roundness and significant abrasion, consistent with long-distance transport (Knight et al. 1999; Garzanti et al. 2012). The volcanic clastic quartz had sharp edges and melting corrosion structures that are indicative of felsic ashfall deposits (Ward 2002). The authigenic quartz precipitated in situ from Si-rich solutions (Dai et al. 2013). The distribution of these features between the cryptocrystalline kaolinitic claystones and tonsteins demonstrates their different origins. Specifically, terrigenous clastic quartz occurred mainly in kaolinitic claystones and were weathered products from the source area that were transported to the study area. Volcanic clastic quartz occurred in tonsteins and is the product of volcanic eruption, with the input of volcanic ash to the study area.

#### Nature of the Parent Rocks

The HFSEs can be used to determine the characteristics of parent rocks (Erkoyun et al. 2019). Zr/Hf ratios were 19.4–37.3 in the cryptocrystalline kaolinitic claystones versus 28–35.23 in the tonsteins, all of which are similar to values for granite (25–41) (Liu et al. 1998), suggesting that the parent rocks of the claystones in the study area were mainly felsic in composition. The Nb/Ta ratio is used commonly as a tracer for magmatic parent rocks (Zhu et al. 2018, 2019). In the present study, the Nb/Ta ratios of the cryptocrystalline kaolinitic claystone and tonstein samples were 9.4–17 and 15.5–19.3, respectively, consistent with felsic parent rocks (Dostal and Chatterjee 2000).

The Al<sub>2</sub>O<sub>3</sub>/TiO<sub>2</sub> ratios are effective indicators of parent rock type for claystones (Spears and Kanaris-Sotiriou 1976; Hayashi et al. 1997; Sugitani et al. 2006), with values of 3–8, 8–21, and 21–70 being characteristic of mafic, intermediate, and felsic sources, respectively (Hayashi et al. 1997; Dai et al. 2017). In the present study, all cryptocrystalline kaolinitic claystones (except WP-39) exhibited TiO<sub>2</sub>-Al<sub>2</sub>O<sub>3</sub> values indicative of a felsic source, whereas the tonstein samples had both felsic and intermediate sources (Fig. 11a). In the ΣREE vs. (La/Yb)<sub>N</sub> discrimination diagram of Allegre and Minster (1978), most cryptocrystalline kaolinitic claystone samples fall into the granite field or overlapping field of granite and sedimentary rocks, with a smaller number of samples falling within the sedimentary rock field, whereas the tonstein samples fall into the overlapping field of basalt and sedimentary rocks (Fig. 11b). These results are consistent with the cryptocrystalline kaolinitic claystones being variably sourced from granite or sedimentary rocks, and the tonsteins being derived from an alkaline basalt source. This finding accounts for the significant

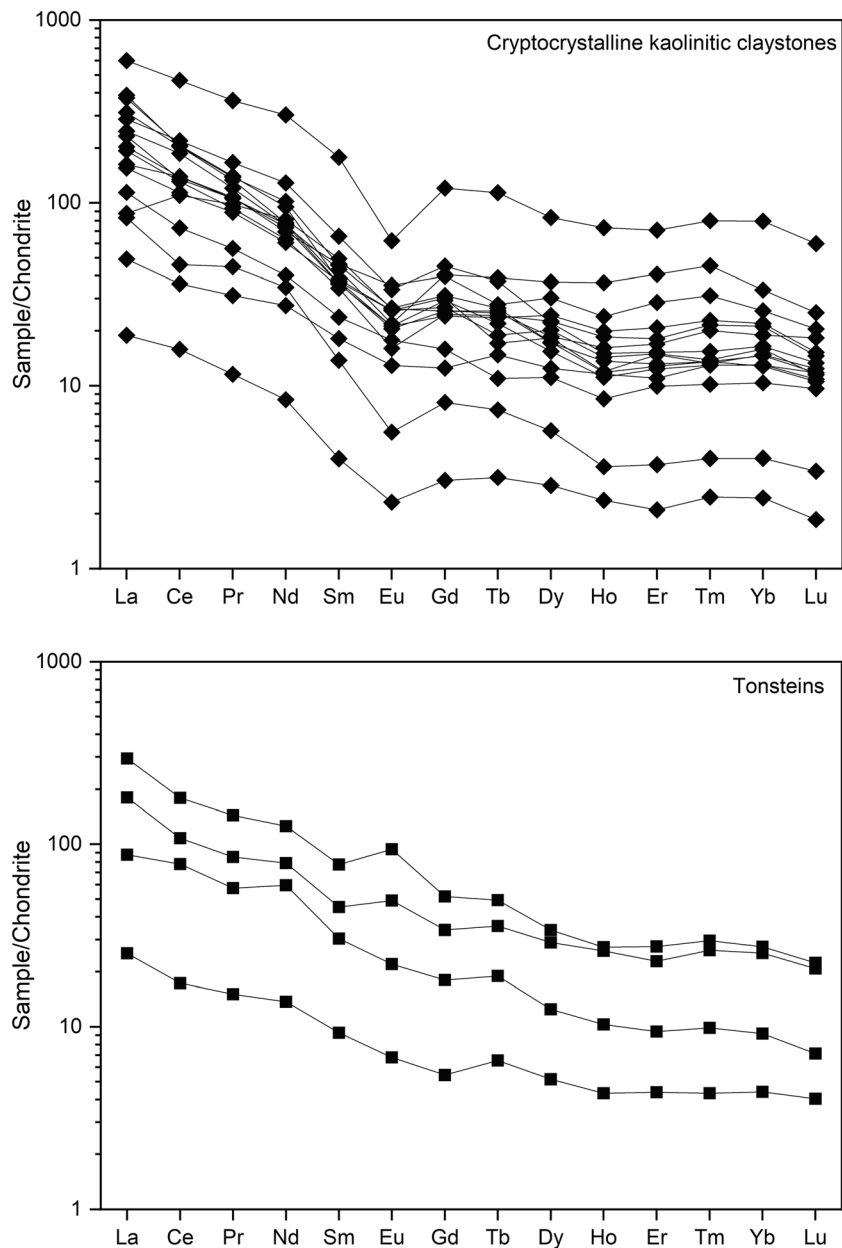


**Fig. 10** Distribution patterns of REE in the cryptocrystalline kaolinitic claystone and tonstein samples of Nanyangpo mine. REE are normalized to chondrite (chondrite data are from McDonough and Sun 1995)

differences in the  $\text{Na}_2\text{O}$  and  $\text{K}_2\text{O}$  compositions of these two types of claystone (Table 5).

The REE patterns have also been used to infer sedimentary rock sources, because mafic rocks have small  $\Sigma\text{LREE}/\Sigma\text{HREE}$  ratios and lack Eu anomalies, whereas more felsic rocks usually contain greater  $\Sigma\text{LREE}/\Sigma\text{HREE}$  ratios and negative Eu anomalies (Baioumy and Gharai 2008). In the present study, the LREE enrichment, HREE depletion, and negative Eu anomalies of most cryptocrystalline kaolinitic claystones confirmed their parent rock as felsic to intermediate igneous rocks or their sedimentary derivatives. Only two tonstein samples showed a weak positive Eu

anomaly, indicating that their parent rock may be alkaline volcanic ash. Furthermore, according to Dai et al. (2014) and Erkoyun et al. (2019), high-temperature hydrothermal fluids circulating through coal deposits after peat accumulation can cause development of a positive Eu anomaly, so the thinness of the tonstein layers may have made them more prone to such diagenetic alteration processes. Although the  $\Sigma\text{REE}$  concentrations in samples WP-8 and WP-17 were markedly lower than other cryptocrystalline kaolinitic claystone samples, these samples exhibited similar chondrite-normalized REE distribution patterns (Fig. 10), which differ somewhat from tonstein samples. In addition, the  $\Sigma\text{REE}$  content in cryptocrystalline

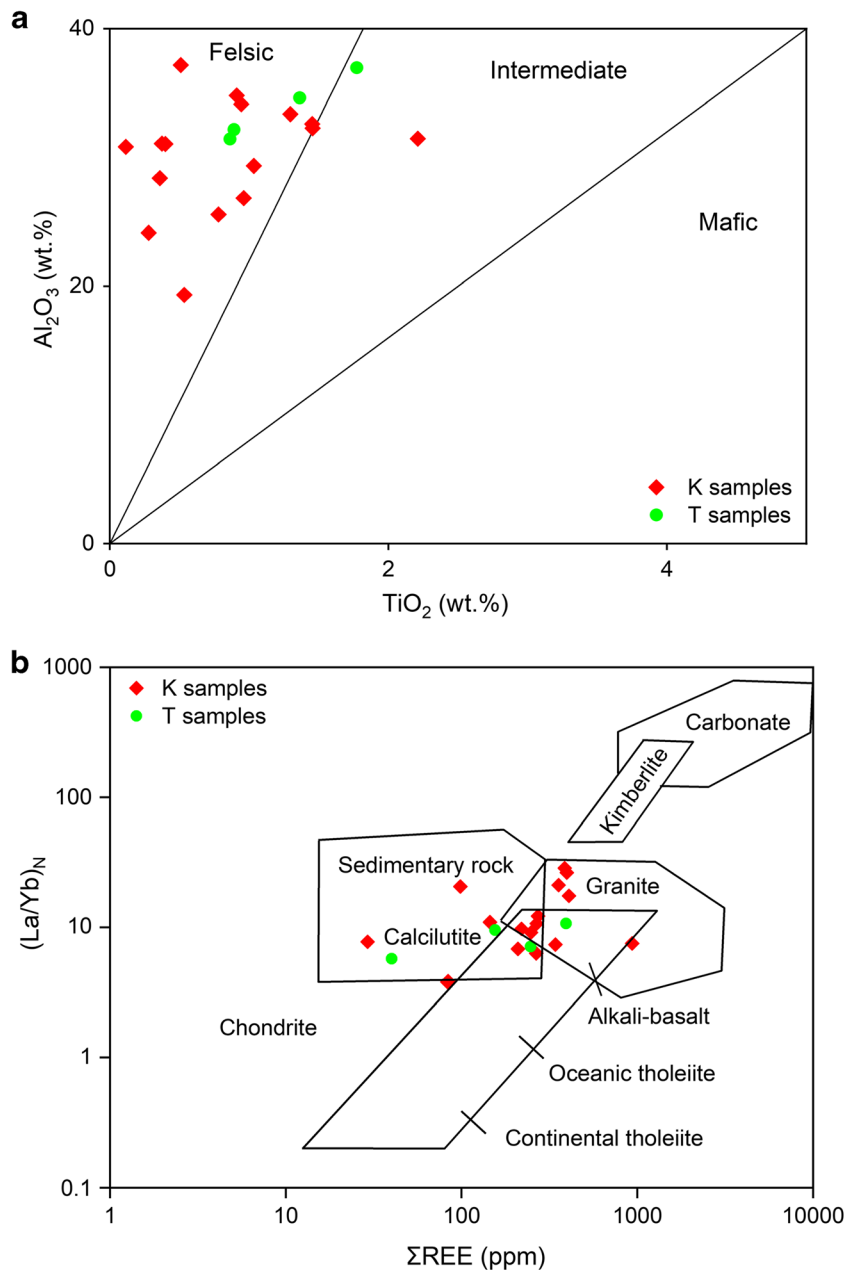


**Fig. 11** Plots of elements in the kaolinitic claystone and tonstein samples from the Nanyangpo mine; **a**: relationship between  $\text{Al}_2\text{O}_3$  and  $\text{TiO}_2$ ; **b**: the  $\Sigma\text{REE}-(\text{La}/\text{Yb})_N$  diagram for the samples (the base map is from Wang et al. 2018); K: cryptocrystalline kaolinitic claystone; T: tonstein

kaolinitic claystones (avg. 291 ppm) was greater than in tonsteins (avg. 215 ppm) (Table 4). Thus, the difference in  $\Sigma\text{REE}$  content and distribution patterns probably indicates that they are from different parent rocks (Hong et al. 2019).

All of the available REE data were normalized to chondrite values (Fig. 12). These data derive from the possible parent rocks of the claystone, which include the Proterozoic metamorphic and magmatic rocks of the Yinshan Block (Liu et al. 2015; Liu 2010) and the Carboniferous volcanic rocks of the Xing'an-Mongolian Orogenic Belt (Fu et al. 2016; Zhou and Jia 2000). Comparison between

distribution patterns of REE (Figs 10 and 12) showed that the chondrite-normalized REE patterns of cryptocrystalline kaolinitic claystones are similar to those of metamorphic and magmatic rocks from the Yinshan Block. This means that these felsic rocks from the Yinshan Block provide metallogenic materials for the formation of claystone, as per the study of Cui (2011). But the parent rocks in the tonsteins are complex, which involves the mixing of volcanic material from the Xing'an-Mongolia Arc and the terrigenous clastic rocks from the adjacent Yinshan Block. As mentioned above, these volcanic materials may be

**Table 5** Student's t-test of kaolinitic claystone samples and tonstein samples

	Kaolinitic claystone	Tonstein	t-test
Major elements (wt %)			
Al <sub>2</sub> O <sub>3</sub>	30.16±4.48	33.80±2.51	t=-1.55, p=0.14
SiO <sub>2</sub>	44.26±9.30	49.99±2.71	t=-1.20, p=0.25
TiO <sub>2</sub>	0.85±0.55	1.22±0.43	t=-1.24, p=0.23
Fe <sub>2</sub> O <sub>3</sub>	2.83±5.10	0.96±0.34	t=0.72, p=0.48
MnO	0.01±0.01	0.00±0.00	t=0.61, p=0.55
MgO	0.29±0.24	0.09±0.03	t=1.66, p=0.12
CaO	0.32±0.26	0.23±0.11	t=0.64, p=0.53
Na <sub>2</sub> O*	0.06±0.03	0.03±0.00	t=3.17, p=0.01
K <sub>2</sub> O**	1.05±0.91	0.17±0.07	t=3.80, p<0.01
P <sub>2</sub> O <sub>5</sub>	0.06±0.06	0.06±0.09	t=0.05, p=0.96
Trace elements (ppm)			
Li	102.89±54.10	123.88±74.91	t=-0.65, p=0.53
Be*	1.85±0.90	1.19±0.17	t=2.78, p=0.01
Sc**	13.74±7.41	21.55±2.55	t=-3.47, p<0.01
V	77.94±58.18	116.93±24.77	t=-1.29, p=0.21
Cr	44.75±37.58	81.68±26.41	t=-1.84, p=0.08
Co	6.23±5.82	5.82±4.40	t=0.13, p=0.90
Ni	22.78±24.04	8.73±3.01	t=1.14, p=0.27
Cu*	26.62±27.85	9.62±1.41	t=2.43, p=0.03
Zn	56.27±20.54	126.83±90.82	t=-1.54, p=0.22
Ga*	33.67±5.90	41.45±3.19	t=-2.51, p=0.02
Rb**	42.52±44.25	5.43±2.20	t=3.34, p<0.01
Sr	85.18±55.90	51.60±20.78	t=1.16, p=0.26
Y	29.84±27.63	28.59±18.89	t=0.09, p=0.93
Mo	2.60±4.81	0.42±0.12	t=0.89, p=0.39
Cd	0.69±1.16	0.14±0.07	t=1.88, p=0.08
In	0.11±0.04	0.09±0.03	t=0.09, p=0.38
Sb*	0.56±0.62	0.06±0.01	t=3.21, p=0.01
Cs*	4.21±5.83	0.44±0.36	t=2.57, p=0.02
Ba	104.18±59.32	77.28±50.75	t=0.83, p=0.42
W	3.75±1.98	2.29±0.58	t=1.44, p=0.17
Pb**	44.40±30.17	12.90±5.25	t=3.95, p<0.01
Tl**	0.35±0.31	0.03±0.02	t=3.96, p<0.01
Bi**	0.51±0.24	0.08±0.07	t=3.53, p<0.01
Th*	25.11±11.96	5.34±1.82	t=3.23, p=0.01
U**	6.74±4.70	1.59±0.66	t=4.23, p<0.01
Nb*	25.52±7.95	13.43±3.53	t=2.92, p=0.01
Ta**	2.15±0.72	0.84±0.20	t=3.56, p<0.01
Zr	346.77±87.51	348.25±131.44	t=-0.03, p=0.98
Hf	11.26±2.59	10.54±3.95	t=0.45, p=0.66
REE	291.42±206.49	208.69±149.16	t=0.75, p=0.47

p < 0.05; \*\* p < 0.01.

imported in the form of volcanic ash. At the same time, these different parent rocks may cause the significant difference in element EFs between the kaolinitic and tonstein samples.

#### *Neoformation of Kaolinite*

This detailed research on the four units of the present study area has established a simplified schematic diagram of the formation model of the kaolinite in the Datong Coalfield

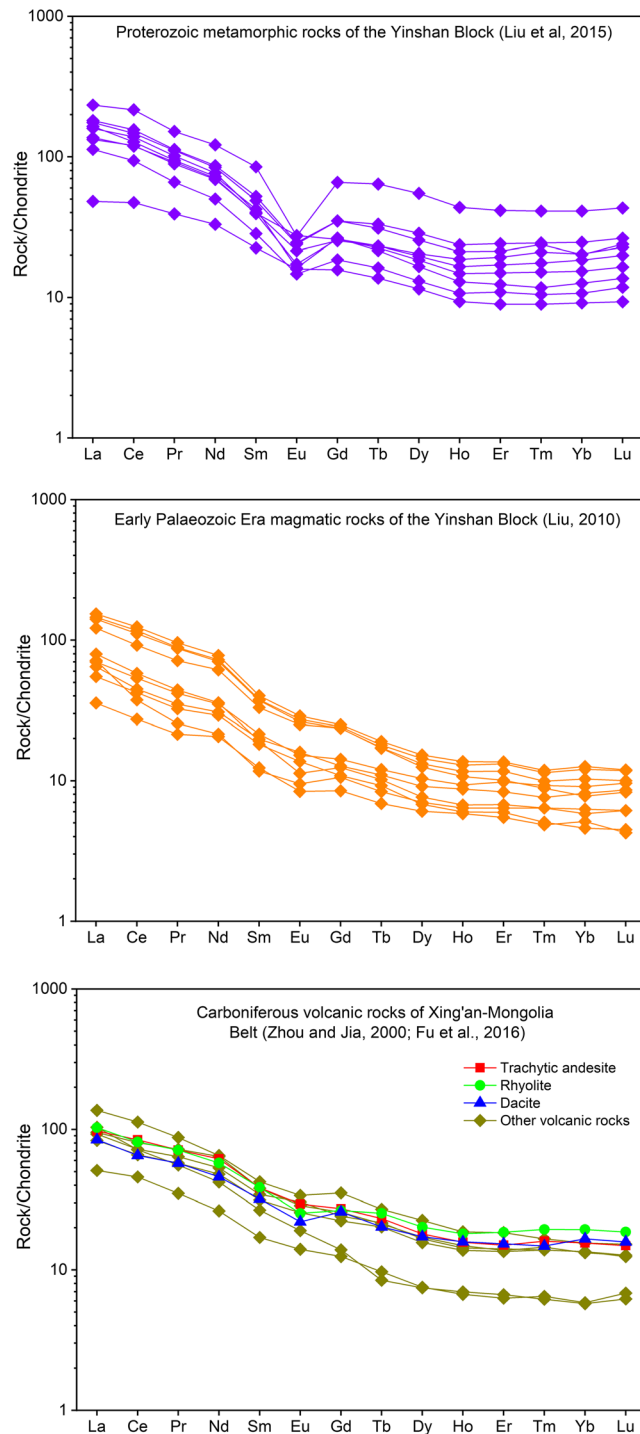


**Fig. 12** Distribution patterns of REE in the probable sources of the studied claystones. REE are normalized to chondrite (McDonough and Sun 1995).

(Fig. 13). Previous studies have shown that the claystones in the coal-bearing strata of the Datong Coalfield were deposited in a plain, with peat swamps developed throughout most of the basin during the Late Paleozoic (Guo and Wang 2005; Xi and Zhao 2011). At the same time, plant residues released large

quantities of organic acids during organic decomposition. This acidic environment facilitated dissolution of Fe, Si, and alkaline ions from original minerals in the parent rock, and provided a suitable environment for the formation of kaolinite (Ding et al. 2009; Zhang et al. 2012). The deposition of terrigenous

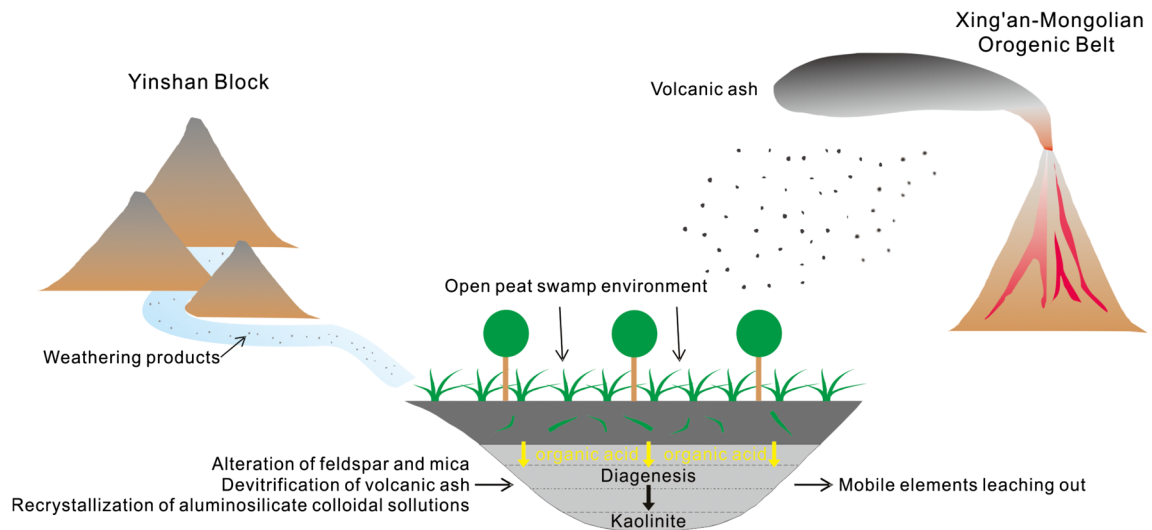


**Fig. 13** Formation model of the kaolinite in the Datong Coalfield

and volcanogenic materials in the swampy environment resulted in transformation of feldspar and mica to kaolinite and volcanic ash to tonsteins, which are overlain and underlain by coal seams (Spears 2012).

The weathering products (terrigenous clastic and colloidal solution) from the Yinshan Block and volcanogenic materials from the Xing'an-Mongolian Orogenic Belt provided the materials for the formation of claystone. The parent rocks rich in aluminosilicate minerals (feldspar and mica, etc.) depleted alkaline metal elements under weathering (Kadir et al. 2014; Gouveia et al. 1993). However, clay minerals such as kaolinite remained, and led to the enrichment of Si, Al, and Fe. These elements are often transported in the form of colloidal solutions (Jin et al. 2015; Kadir et al. 2014). These terrigenous clastic grains and kaolinite aggregates are oriented, showing the characteristics of water flow (Liu et al. 2019). Therefore, those weathering products were transported to peat swamp under hydrodynamic conditions. The volcanic ashes were transported by air, however, and fell into the peat swamp sedimentary basin.

## CONCLUSIONS

The Nanyangpo mine provides an excellent opportunity to improve understanding of the diagenetic process of kaolinitic claystone because it has two different types of kaolinitic claystone deposits, each with its own kaolinite identity. An integrated study on the mineralogy, chemical compositions, and textures of the claystone sediments showed that claystones associated with coal seams in the Datong Coalfield formed from terrigenous clastics, aluminosilicate colloidal solution, and volcanic ash in a swampy peaty coal environment, and the climate was hot and humid. These claystones occur on the roof, floor, or partings of the coal seams; their main mineral component is kaolinite, associated with illite, quartz, pyrite, anatase, feldspar, siderite, and calcite. The development of vermicular kaolinite crystals suggest a diagenetic origin. The

well-ordered, vermiform and plate-like morphological kaolinites formed authigenically from alteration of feldspar and mica and appear in both cryptocrystalline kaolinitic claystone and tonstein. A kaolinite matrix and aggregates in cryptocrystalline kaolinitic claystone and tonstein formed by recrystallization of aluminosilicate colloidal solution and volcanic vitric fragment, respectively. In contrast, the kaolinite in tonstein has a greater degree of order.

The  $Al_2O_3/TiO_2$ , Zr/Hf, and Nb/Ta ratios indicate that the parent rocks were felsic. The presence of volcanic quartz and vitric fragment indicates the input of volcanic ash. The chondrite-normalized REE patterns show that the parent rocks were metamorphic and magmatic rocks from the Yinshan Block, and volcanic material from the Xing'an-Mongolian Orogenic Belt. The high CIA values indicate intensive chemical weathering and an open acidic, hydrologic system. The U/Th ratios and the EFs of V, U, and Mo suggest a suboxic to anoxic environment. The leaching of Si+Fe and alkaline ions favored the formation of kaolinite under acidic conditions. The high  $\Sigma LREE/\Sigma HREE$  ratios, negative Eu anomalies, and depletion of Rb, Cs, Sr, and Ba resulted from alteration of feldspar and mica, or transportation from sediment source to the swamp peat area under reducing conditions. The correlation coefficients of the elements indicate that the REE occurred in the feldspar or mica minerals of the parent rocks, and the  $\Sigma REE$  content decreased with the alteration of feldspar minerals to kaolinite. The  $\Sigma REE$  content in cryptocrystalline kaolinitic claystone is greater than that in tonstein, which is caused by the difference in parent rocks. Overall, the formation of coal-bearing claystone is restricted mainly by two factors, one being the parent rocks and the other being the alteration and recrystallization during diagenesis.

## ACKNOWLEDGMENTS

This study was funded by the National Key R&D Program of China (No. 2019YFC1904903) and the Science and Technology

Major Projects of Shanxi Province of China (No. 20181101003). The authors would like to thank the editor-in-chief Prof. Joseph W. Stucki, associate editor Prof. Selahattin Kadir, and the other anonymous reviewer for their careful comments on the manuscript, which greatly improved the quality of the paper. The authors are also grateful to Editors Kevin Murphy and Robert Preston for handling and editing the manuscript.

## FUNDING

Funding sources are as stated in the Acknowledgments.

## Declarations

## Conflict of Interest

The authors declare that they have no conflict of interest.

## REFERENCES

- Algeo, T. J., & Liu, J. (2020). A re-assessment of elemental proxies for paleoredox analysis. *Chemical Geology*, 119549.
- Algeo, T. J., & Tribovillard, N. (2009). Environmental analysis of paleoceanographic systems based on molybdenum–uranium covariation. *Chemical Geology*, 268, 211–225.
- Algeo, T. J., Hinnov, L., Moser, J., Maynard, J. B., Elswick, E., Kuwahara, K., & Sano, H. (2010). Changes in productivity and redox conditions in the Panthalassic Ocean during the latest Permian. *Geology*, 38, 187–190.
- Allegre, C., & Minster, J. (1978). Quantitative models of trace element behavior in magmatic processes. *Earth and Planetary Science Letters*, 38, 1–25.
- Arbuzov, S. I., Mezhibor, A. M., Spears, D., Ilenok, S. S., Shaldybin, M. V., & Belaya, E. (2016). Nature of tonsteins in the Azeisk deposit of the Irkutsk Coal Basin (Siberia, Russia). *International Journal of Coal Geology*, 153, 99–111.
- Baioumy, H., & Gharaie, M. (2008). Characterization and origin of late Devonian illitic clay deposits southwestern Iran. *Applied Clay Science*, 42, 318–325.
- Bauluz, B., Mayayo, M., Yuste, A., & González López, J. (2008). Genesis of kaolinite from Albian sedimentary deposits of the Iberian Range (NE Spain): analysis by XRD, SEM and TEM. *Clay Minerals*, 43, 459–475.
- Bohor, B. F., & Triplehorn, D. M. (1993). *Tonsteins: altered volcanic ash layers in coal-bearing sequences*. In *Special Paper* (Vol. Special Paper 285, p. 285). Geological Society of America.
- Brindley, G., & Brown, G. (1980). Quantitative X-ray mineral analysis of clays. *Crystal structures of clay minerals and their X-ray identification, Mineralogical Society Monograph*, 5, 411–438.
- Burger, K., Zhou, Y., & Ren, Y. (2002). Petrography and geochemistry of tonsteins from the 4th Member of the Upper Triassic Xujiahe formation in southern Sichuan Province, China. *International Journal of Coal Geology*, 49, 1–17.
- Burton, J. H., & Price, T. D. (1990). The ratio of barium to strontium as a paleodietary indicator of consumption of marine resources. *Journal of Archaeological Science*, 17, 547–557.
- Cheng, Y., Yang, Z., Fan, E., Zhao, J., Gao, Y., Sun, D., & Wang, C. (2015). Coal-accumulating processes and base level cycles of the Taiyuan Formation in the Datong coalfield. *Geology in China (in Chinese with English abstract)*, 042(006), 1959–1968.
- Cui, X. (2011). Analysis of the source of the deposits of Datong Coal seams formed in the Permo-Carboniferous Period. *Journal of Shanxi Datong University (Natural Science Edition)*, 27, 55–58.
- Dai, S., Wang, X., Zhou, Y., Hower, J. C., Li, D., Chen, W., Zhu, X., & Zou, J. (2011). Chemical and mineralogical compositions of silicic, mafic, and alkali tonsteins in the late Permian coals from the Songzao Coalfield, Chongqing, Southwest China. *Chemical Geology*, 282, 29–44.
- Dai, S., Zhang, W., Seredin, V. V., Ward, C. R., Hower, J. C., Song, W., Wang, X., Li, X., Zhao, L., & Kang, H. (2013). Factors controlling geochemical and mineralogical compositions of coals preserved within marine carbonate successions: a case study from the Heshan Coalfield, southern China. *International Journal of Coal Geology*, 109, 77–100.
- Dai, S., Li, T., Seredin, V. V., Ward, C. R., Hower, J. C., Zhou, Y., Zhang, M., Song, X., Song, W., & Zhao, C. (2014). Origin of minerals and elements in the Late Permian coals, tonsteins, and host rocks of the Xinde Mine, Xuanwei, eastern Yunnan, China. *International Journal of Coal Geology*, 121, 53–78.
- Dai, S., Xie, P., Jia, S., Ward, C. R., Hower, J. C., Yan, X., & French, D. (2017). Enrichment of U-Re-V-Cr-Se and rare earth elements in the Late Permian coals of the Moxinpo Coalfield, Chongqing, China: Genetic implications from geochemical and mineralogical data. *Ore Geology Reviews*, 80, 1–17.
- Dalai, T. K., Rengarajan, R., & Patel, P. P. (2004). Sediment geochemistry of the Yamuna River System in the Himalaya: Implications to weathering and transport. *Geochemical Journal*, 38, 441–453.
- Ding, S. L., Liu, Q., & Wang, M. (2009). Study of kaolinite rock in coal bearing stratum, North China. *Procedia Earth and Planetary Science*, 1, 1024–1028.
- Dominguez, E., Iglesias, C., & Dondi, M. (2008). The geology and mineralogy of a range of kaolins from the Santa Cruz and Chubut Provinces, Patagonia (Argentina). *Applied Clay Science*, 40, 124–142.
- Dostal, J., & Chatterjee, A. (2000). Contrasting behaviour of Nb/Ta and Zr/Hf ratios in a peraluminous granitic pluton (Nova Scotia, Canada). *Chemical Geology*, 163, 207–218.
- Ece, O. I., Nakagawa, Z., & Schroeder, P. (2003). Alteration of volcanic rocks and genesis of kaolin deposits in the Sile Region, northern Istanbul, Turkey. I: Clay mineralogy. *Clay Minerals*, 38, 529–550.
- Eggleton, R. A., Foudoulis, C., & Varkevisser, D. (1987). Weathering of basalt: Changes in rock chemistry and mineralogy. *Clays and Clay Minerals*, 35, 161–169.
- Erkoyun, H., Kadir, S., Külah, T., & Huggett, J. (2017). Mineralogy, geochemistry and genesis of clays interlayered coal seams succession in the Neogene lacustrine Seyitömer coal deposit, Kütahya, Western Turkey. *International Journal of Coal Geology*, 172, 112–133.
- Erkoyun, H., Kadir, S., & Huggett, J. (2019). Occurrence and genesis of tonsteins in the Miocene lignite, Tunçbilek Basin, Kütahya, Western Turkey. *International Journal of Coal Geology*, 202, 46–68.
- Fu, D., Huang, B., Peng, S., Kusky, T. M., Zhou, W., & Ge, M. (2016). Geochronology and geochemistry of late Carboniferous volcanic rocks from northern Inner Mongolia, North China: Petrogenesis and tectonic implications. *Gondwana Research*, 36, 545–560.
- Galán, E., Aparicio, P., Fernández-Caliani, J. C., Miras, A., Márquez, M. G., Fallick, A. E., & Clauer, N. (2016). New insights on mineralogy and genesis of kaolin deposits: The Burela kaolin deposit (Northwestern Spain). *Applied Clay Science*, 131, 14–26.
- Garzanti, E., Andò, S., Vezzoli, G., Lustrino, M., Boni, M., & Vermeesch, P. (2012). Petrology of the Namib Sand Sea: long-distance transport and compositional variability in the wind-displaced Orange Delta. *Earth-Science Reviews*, 112, 173–189.
- Gong, L. (2006). Evolution research of Datong Late Paleozoic coal-bearing basin. Taiyuan University of Technology (in Chinese with English abstract).
- Gotze, J., Plötze, M., & Habermann, D. (2001). Origin, spectral characteristics and practical applications of the cathodoluminescence (CL) of quartz—a review. *Mineralogy and Petrology*, 71, 225–250.
- Gouveia, M., Prudencio, M., Figueiredo, M., Pereira, L. J., & Waerenborgh, J. (1993). Behavior of REE and other trace and major elements during weathering of granitic rocks, Evora, Portugal. *Chemical Geology*, 107, 293–296.



- Guo, H., & Wang, Y. (2005). Geochemical characteristics of shallow groundwater in Datong basin, Northwestern China. *Journal of Geochemical Exploration*, 87, 109–120.
- Han, Z., Song, Z., Gao, L., Guo, Z., Liu, G., & Zhong, W. (2014). Advances of sedimentary characteristics and basin evolution of Paleozoic in the North Eastern Margin of the North China Block. *Journal of Shandong University of Science & Technology*, 33, 1–10 (in Chinese with English abstract).
- Hayashi, K. I., Fujisawa, H., Holland, H. D., & Ohmoto, H. (1997). Geochemistry of ~19. Ga sedimentary rocks from northeastern Labrador, Canada. *Geochimica et Cosmochimica Acta*, 61, 4115–4137.
- He, S. (2006). Mass origin and genesis of claystone in Tashan Coalmine, Datong. *Coal Geology of China*, 18(3), 23–25.
- Hong, H., Zhao, L., Fang, Q., Algeo, T. J., Wang, C., Yu, J., Gong, N., Yin, K., & Ji, K. (2019). Volcanic sources and diagenetic alteration of Permian–Triassic boundary K-bentonites in Guizhou Province, South China. *Palaeogeography, Palaeoclimatology, Palaeoecology*, 519, 141–153.
- Huo, S. (2013). *The measures of kaolinite mineral characteristics and occurrence regularity in Datong coal mining area*. Taiyuan University of Technology.
- Hou, H., Shao, L., Wang, S., Xiao, Z., Wang, X., Li, Z., & Mu, G. (2019). Influence of depositional environment on coalbed methane accumulation in the Carboniferous-Permian coal of the Qinshui Basin, northern China. *Frontiers of Earth Science*, 13, 535–550.
- Jin, Z., Zhou, J., Huang, Z., Xie, X., Jing, G. U., Liu, L., et al. (2015). Mineralogical characteristics of the bauxite deposit in the Wuchuan-Zheng'an-Daozhen Area, northern Guizhou Province, China. *Acta Geologica Sinica*, 089, 1458–1470.
- Kadir, S., & Akbulut, A. (2009). Mineralogy, geochemistry and genesis of the Taşoluk kaolinite deposits in pre-Early Cambrian metamorphites and Neogene volcanites of Afyonkarahisar, Turkey. *Clay Minerals*, 44, 89–112.
- Kadir, S., & Erkoyun, H. (2013). Genesis of the hydrothermal Karaçayır kaolinite deposit in Miocene volcanics and Palaeozoic metamorphic rocks of the Uşak-Güre Basin, western Turkey. *Turkish Journal of Earth Sciences*, 22, 444–468.
- Kadir, S., Erman, H., & Erkoyun, H. (2011). Mineralogical and geochemical characteristics and genesis of hydrothermal kaolinite deposits within Neogene volcanites, Kütahya (western Anatolia). Turkey. *Clays and Clay Minerals*, 59, 250–276.
- Kadir, S., Külah, T., Eren, M., Önalgil, N., & Gürel, A. (2014). Mineralogical and geochemical characteristics and genesis of the Güzeyurt alunite-bearing kaolinite deposit within the Late Miocene Gördeles ignimbrite, Central Anatolia, Turkey. *Clays and Clay Minerals*, 62, 477–499(423).
- Kang, J. (2015). *Distribution of elements and enrichment mechanism of mineral matter in the Wuhai C-P coals*. Beijing: China University of Mining and Technology (in Chinese with English abstract).
- Knight, J., Morison, S., & Mortensen, J. (1999). The relationship between placer gold particle shape, rimming, and distance of fluvial transport as exemplified by gold from the Klondike District, Yukon Territory, Canada. *Economic Geology*, 94, 635–648.
- Li, C. (1981). Contour of plate tectonics in China. *Geology and Prospecting*, 2(8), 13–21+132 (in Chinese with English abstract).
- Li, X. (2015). *Mineral matter characteristic and sources of volcanic ash in the Late Permian coal-bearing strata from Xuanwei, eastern Yunnan*. Beijing: China University of Mining and Technology (in Chinese with English abstract).
- Liu, C. L. (1984). So called "black sandy stone" origin of coarse grain kaolinite. *Journal of Mineralogy and Petrology*, 4, 57–65.
- Liu, C. F. (2010). *Paleozoic–Early Mesozoic magmatic belts and tectonic significance in Siziwangqi area, Inner Mongolia*. Beijing: China University of Geosciences.
- Liu, Q., & Zhang, P. (1997). *The Composition and Mineralization Mechanism of Kaolinite Rocks in Late-Palaeozoic Coal Measures, North China*. Beijing: Marine Press.
- Liu, Q., Yang, X., & Ding, S. (1998). Geochemistry of trace elements and REE on kaolinite rocks in Late-Paleozoic measures, North China. *Geochimica*, 2, 196–203.
- Liu, Q., Spears, D., Zhang, P., & Xu, H. (2001). The origins of kaolinite-rich rocks associated with coal measures in China. *Clay Minerals*, 36, 389–402.
- Liu, J., Liang, S., Xiao, R., & Zhang, Y. (2015). Geochemistry, geochronology and petrogenesis of the ore-forming intrusive body in the Baoyintu molybdenum deposit, Inner Mongolia. *Geology in China*, 42, 149–168 (in Chinese with English abstract).
- Liu, Q., Liu, D., Ding, S., Liu, L., & Zhang, T. (2019). Origin of kaolinite rocks under Coal No.9 of Taiyuan Formation in Datong coalfield. *Journal of Hebei University of Engineering (Natural Science Edition)*, 36(2), 64–69.
- Liu, J., Cao, D., Zhang, Y., & Li, Y. (2020a). Temporal changes in an epeiric paralic deposition during a third-order relative sea-level cycle (Late Pennsylvanian, western North China): Insights from integrated facies and sequence stratigraphic analysis. *Journal of Asian Earth Sciences*, 104349.
- Liu, L., Zhang, T., Liu, J., Liu, Q., Li, K., Liu, D., & Liu, W. (2020b). Genesis of kaolinite deposits in Junggar Coalfield, North China: Petrological, mineralogical and geochemical evidence. *Acta Geologica Sinica-English Edition*. <https://doi.org/10.1111/17556724.14527>.
- Lopez, J. M. G., Bauluz, B., Fernández-Nieto, C., & Oliete, A. Y. (2005). Factors controlling the trace-element distribution in fine-grained rocks: the Albian kaolinite-rich deposits of the Oliete Basin (NE Spain). *Chemical Geology*, 214, 1–19.
- Martinez-Ruiz, F., Kastner, M., Gallego-Torres, D., Rodrigo-Gámiz, M., Nieto-Moreno, V., & Ortega-Huertas, M. (2015). Paleoclimate and paleoceanography over the past 20,000 yr in the Mediterranean Sea Basins as indicated by sediment elemental proxies. *Quaternary Science Reviews*, 107, 25–46.
- McDonough, W. F., & Sun, S. S. (1995). The composition of the Earth. *Chemical Geology*, 120, 223–253.
- McLennan, S. M. (2001). Relationships between the trace element composition of sedimentary rocks and upper continental crust. *Geochemistry, Geophysics, Geosystems*, 2(4).
- Mongelli, G. (1997). Ce-anomalies in the textural components of Upper Cretaceous karst bauxites from the Apulian carbonate platform (southern Italy). *Chemical Geology*, 140, 69–79.
- Moore, D. M., & Reynolds, R. C. (1989). *X-ray Diffraction and the Identification and Analysis of Clay Minerals*. New York: Oxford University Press.
- Nesbitt, H. W., & Young, G. (1982). Early Proterozoic climates and plate motions inferred from major element chemistry of lutites. *Nature*, 299(5885), 715–717.
- Nzeugang, A. N., El Ouahabi, M., Aziwo, B., Mache, J., Mouton, H. M., & Fagel, N. (2018). Characterization of kaolin from Mankon, Northwest Cameroon. *Clay Minerals*, 53, 563–577.
- Panahi, A., Young, G. M., & Rainbird, R. H. (2000). Behavior of major and trace elements (including REE) during Paleoproterozoic pedogenesis and diagenetic alteration of an Archean granite near Ville Marie, Québec, Canada. *Geochimica et Cosmochimica Acta*, 64, 2199–2220.
- Price, N. B., & Duff, P. M. D. (1969). Mineralogy and chemistry of tonsteins from Carboniferous sequences in Great Britain. *Sedimentology*, 13, 45–69.
- Ruppert, L. F., & Moore, T. A. (1993). Differentiation of volcanic ash-fall and water-borne detrital layers in the Eocene Senakin coal bed, Tanjung Formation, Indonesia. *Organic Geochemistry*, 20, 233–247.
- Spears, D. (2012). The origin of tonsteins, an overview, and links with seatearths, fireclays and fragmental clay rocks. *International Journal of Coal Geology*, 94, 22–31.
- Spears, D., & Kanaris-Sotiriou, R. (1976). Titanium in some Carboniferous sediments from Great Britain. *Geochimica et Cosmochimica Acta*, 40, 345–351.
- Sugitani, K., Yamashita, F., Nagaoka, T., Yamamoto, K., Minami, M., Mimura, K., & Suzuki, K. (2006). Geochemistry and sedimentary

- petrology of Archean clastic sedimentary rocks at Mt. Goldsworthy, Pilbara Craton, Western Australia: evidence for the early evolution of continental crust and hydrothermal alteration. *Precambrian Research*, 147, 124–147.
- Taboada, T., Cortizas, A. M., García, C., & García-Rodeja, E. (2006). Uranium and thorium in weathering and pedogenetic profiles developed on granitic rocks from NW Spain. *Science of the Total Environment*, 356, 192–206.
- Tauler, E., Xu, J., Campeny, M., Amores, S., Melgarejo, J. C., Martínez, S., & Gonçalves, A. O. (2019). A new kaolin deposit in Western Africa: Mineralogical and compositional features of kaolinite from Caluquembe (Angola). *Clays and Clay Minerals*, 67, 228–243.
- Taylor, S. R., & McLennan, S. M. (1985). *The Continental Crust: Its Composition and Evolution*. USA.
- Tribouillard, N., Algeo, T. J., Lyons, T., & Riboulleau, A. (2006). Trace metals as paleoredox and paleoproductivity proxies: an update. *Chemical Geology*, 232, 12–32.
- Triplehorn, D. M., Stanton, R. W., Ruppert, L. F., & Crowley, S. S. (1991). Volcanic ash in the Wyodak-Anderson coal bed, Powder River basin, Wyoming. *Organic Geochemistry*, 17, 567–575.
- Uysal, I. T., Golding, S. D., & Audsley, F. (2000). Clay-mineral authigenesis in the Late Permian Coal Measures, Bowen Basin, Queensland, Australia. *Clays and Clay Minerals*, 48, 351–365.
- Wang, J., & Guo, S. (2020). Comparison of geochemical characteristics of marine facies, marine-continental transitional facies and continental facies shale in typical areas of china and their control over organic-rich shale. *Energy Sources, Part A: Recovery, Utilization, and Environmental Effects*, 1–13.
- Wang, X., Wang, G., Zhou, J., Cui, Y., Zhang, D., Li, W., & Fan, L. (2013). REE characteristics of the Datie bauxite deposit in Qiubei County, southeast Yunnan Province. *Acta Geoscientia Sinica*, 34(s1), 127–134.
- Wang, G., Xie, Y., Qin, Y., Wang, J., Shen, J., Han, B., Liang, C., & Wang, Q. (2018). Element geochemical characteristics and formation environment for the roof, floor and gangue of coal seams in the Gujiao mining area, Xishan coalfield, China. *Journal of Geochemical Exploration*, 190, 336–344.
- Ward, C. R. (2002). Analysis and significance of mineral matter in coal seams. *International Journal of Coal Geology*, 50, 135–168.
- Wei, W., & Algeo, T. J. (2020). Elemental proxies for paleosalinity analysis of ancient shales and mudrocks. *Geochimica et Cosmochimica Acta*, 287, 341–366.
- Wei, W., Algeo, T. J., Lu, Y., Lu, Y., Liu, H., Zhang, S., Peng, L., Zhang, J., & Chen, L. (2018). Identifying marine incursions into the Paleogene Bohai Bay Basin lake system in northeastern China. *International Journal of Coal Geology*, 200, 1–17.
- Wilkin, R., & Barnes, H. (1997). Formation processes of framboidal pyrite. *Geochimica et Cosmochimica Acta*, 61, 323–339.
- Xi, B., & Zhao, W. (2011). Tectonic setting analysis of Datong Coalfield Carboniferous provenance in Shanxi. *Coal Geology of China*, 23(09), 14–18 (in Chinese with English abstract).
- Yuan, Y., Cao, D. Y., Lin, Z. Y., & Liu, K. (2011). Study on structural coal-control characteristics in Datong coalfield. *Coal Geology of China*, 23(8), 63–65.
- Zhang, H. (1992). Shape-genesis types of the kaolinites in coal series. *Acta Mineralogica Sinica*, 12, 53–57.
- Zhang, Y., & Zhao, S. (1990). The sedimentary environment of the late Paleozoic coal-bearing series in Datong coalfield. *Shanxi Mining Institute Learend Journal*, 4, 357–362 (in Chinese with English abstract).
- Zhang, L., Luo, L., & Zhang, S. (2012). Integrated investigations on the adsorption mechanisms of fulvic and humic acids on three clay minerals. *Colloids & Surfaces A Physicochemical & Engineering Aspects*, 406, 84–90.
- Zhao, X., & Zheng, J. (1997). Depositional characteristics and sequence stratigraphic significance of late paleozoic coal-bearing strata in Datong, Shanxi. *Geological Review*, 43(01), 85–90 (in Chinese with English abstract).
- Zhao, L., Ward, C. R., French, D., Graham, I. T., Dai, S., Yang, C., Xie, P., & Zhang, S. (2018). Origin of a kaolinite-NH<sub>4</sub>-illite-pyrophyllite-chlorite assemblage in a marine-influenced anthracite and associated strata from the Jincheng Coalfield, Qinshui Basin, Northern China. *International Journal of Coal Geology*, 185, 61–78.
- Zhao, L., Dai, S., Nechaev, V. P., Nechaeva, E. V., Graham, I. T., French, D., & Sun, J. (2019). Enrichment of critical elements (Nb-Ta-Zr-Hf-REE) within coal and host rocks from the Datanhao mine, Daqingshan Coalfield, northern China. *Ore Geology Reviews*, 102951.
- Zhou, A. (2010). *Research on Geology of Datong Late Paleozoic Coal-bearing Basin*. Beijing: China Coal Industry Publishing House.
- Zhou, A. C., & Jia, B. W. (2000). Analysis of Late Paleozoic conglomerates from Daqing Mountain in Inner Mongolia. *Journal of Taiyuan University of technology*, 31, 498–504.
- Zhu, R. (1997). Geochemical discriminant criteria of the genesis of kaolin rocks in coal measures. *Geological Review*, 2, 11–20.
- Zhu, Z., Wang, R., Maignac, C., Cuney, M., Mercadier, J., Che, X., & Lespinasse, M.-Y. (2018). A new style of rare metal granite with Nb-rich mica: The Early Cretaceous Huangshan rare-metal granite suite, northeast Jiangxi Province, Southeast China. *American Mineralogist*, 103, 1530–1544.
- Zhu, Q., Feng, X., Li, J., Sima, X., Tang, C., Xu, Z., Liu, X., Si, Q., Li, G., & Wen, S. (2019). Mineralogy, geochemistry, and fluid action process of uranium deposits in the Zhiluo Formation, Ordos Basin, China. *Ore Geology Reviews*, 111, 102984.
- Zielinski, R. A. (1985). Element mobility during alteration of silicic ash to kaolinite—a study of tonstein. *Sedimentology*, 32, 567–579.
- Zou, Y., Liu, D., & Liu, H. (2016). Occurrence characteristics of chemical elements of No. 5 coal in Taiyuan Formation of Datong Coal Field. *Coal Science and Technology*, (S1), 167–172 (in Chinese with English abstract).

(Received 30 June 2020; revised 18 December 2020; AE: Selahattin Kadir)